ELSEVIER

Contents lists available at ScienceDirect

# Remote Sensing of Environment

journal homepage: www.elsevier.com/locate/rse



# Mapping regional turbulent heat fluxes via variational assimilation of land surface temperature data from polar orbiting satellites



Tongren Xu<sup>a,\*</sup>, Xinlei He<sup>a</sup>, Sayed M. Bateni<sup>b</sup>, Thomas Auligne<sup>c,d</sup>, Shaomin Liu<sup>a</sup>, Ziwei Xu<sup>a</sup>, Ji Zhou<sup>e</sup>, Kebiao Mao<sup>f</sup>

- <sup>a</sup> State Key Laboratory of Earth Surface Processes and Resource Ecology, School of Natural Resources, Faculty of Geographical Science, Beijing Normal University, Beijing 100875 China
- b Department of Civil and Environmental Engineering and Water Resources Research Center, University of Hawaii at Manoa, Honolulu, HI, USA
- <sup>c</sup> Joint Center for Satellite Data Assimilation, MD, USA
- <sup>d</sup> University Corporation for Atmospheric Research, CO, USA
- e School of Resources and Environment, Center for Information Geoscience, University of Electronic Science and Technology of China, Chengdu 611731, China
- <sup>f</sup> National Hulunber Grassland Ecosystem Observation and Research Station, Institute of Agricultural Resources and Regional Planning, Chinese Academy of Agricultural Sciences, Beijing 100081, China

#### ARTICLE INFO

#### Keywords: Variational data assimilation Land surface temperature Sensible heat flux Latent heat flux MODIS

#### ABSTRACT

Estimation of turbulent heat fluxes by assimilating sequences of land surface temperature (LST) measurements into variational data assimilation (VDA) frameworks has been the subject of several studies. The VDA approaches estimate turbulent heat fluxes by minimizing the difference between LST observations and estimations from the heat diffusion equation. The VDA methods have been tested only with high temporal resolution LST observations (e.g., from geostationary satellites) when applied at regional scales. Geostationary satellites can capture the diurnal cycle of LST, but they have a relatively low spatial resolution and mainly focus on low latitudes. To overcome these shortcomings, this study assimilates high spatial resolution LST data from polar orbiting satellites (e.g., Moderate Resolution Imaging Spectroradiometer, MODIS) into the combined-source (CS) and dualsource (DS) VDA schemes. An expression is developed to obtain an a priori evaporative fraction (EF) estimate from leaf area index (LAI) or apparent thermal inertia (ATI). The a priori EF estimate is used as an initial guess in the VDA approach. The results indicate that the VDA method is able to find the optimal value of EF by assimilating the low-temporal resolution MODIS LST data. The predicted turbulent heat fluxes from VDA are compared with the measurements from the large-aperture scintillometer at three sites (Arou, Daman, and Sidaoqiao) in the Heihe River Basin (located in northwest China). The findings indicate that the CS and DS VDA models perform well in various hydrological and vegetative conditions. The three-site-average root mean square errors (RMSEs) of sensible and latent heat fluxes estimates from the CS scheme are  $37.44 \, \mathrm{W \, m^{-2}}$  and  $94.30 \, \mathrm{W \, m^{-2}}$ . respectively. The DS model reduces the abovementioned RMSEs by 19.82% and 21.37%, respectively. Overall, the results show that using the a priori EF estimate from the proposed expression in the VDA approach eliminates the need for the high resolution LST data from geostationary satellites, and allows the VDA method to estimate turbulent heat fluxes by assimilating LST data from polar orbiting satellites. Finally, several numerical tests are conducted to assess the effect of LST temporal sampling on the turbulent heat fluxes estimates. The results show that the LST measurement at 1400 Local Time (LT) has the most amount of information for partitioning the available energy into sensible and latent heat fluxes.

#### 1. Introduction

The sensible (*H*) and latent (LE) heat fluxes affect the land-atmosphere interaction and boundary layer development. Their accurate estimation is required for the efficient use and management of water

resources, irrigation scheduling, and weather prediction (Bastiaanssen et al., 2005; Williams et al., 2016; Li et al., 2017; Ma et al., 2018). Turbulent heat fluxes can be measured by different techniques such as the eddy covariance system, lysimeter, Bowen ratio method, and large-aperture scintillometer (Liu et al., 2016). These measurements have

<sup>\*</sup> Corresponding author at: State Key Laboratory of Earth Surface Processes and Resource Ecology, School of Natural Resources, Faculty of Geographical Science, Beijing Normal University, No. 19, Xinjiekouwai Street, Beijing 100875, China.

E-mail address: xutr@bnu.edu.cn (T. Xu).

limited spatial and temporal coverage. Thus, various models have been developed to estimate turbulent heat fluxes over large-scale domains.

Bateni and Entekhabi (2012a) showed that sequences of land surface temperature (LST) observations contain implicit information on the partitioning of the available energy among the surface energy balance (SEB) components. LST observations have been utilized in five main groups of studies to estimate turbulent heat fluxes. The first group uses LST to solve the SEB equation and estimate the surface energy fluxes (Bastiaanssen et al., 1998a, 1998b; Su, 2002; Liu et al., 2007; Jia et al., 2009; Song et al., 2016a; Ma et al., 2018). The second group attempts to estimate the latent heat flux by using the empirical relationship between LST and vegetation indices such as normalized differential vegetation index (NDVI), leaf area index (LAI), etc. (Jiang and Islam, 2001, 2003; Nishida et al., 2003; Wang et al., 2006; Tang et al., 2010; Sun et al., 2013; Zhu et al., 2017). The third group incorporates LST observations into the Penman-Monteith equation to estimate turbulent heat fluxes (Mallick et al., 2013, 2014). The fourth group (known as the land data assimilation system [LDAS]) estimates surface heat fluxes by the ensemble Kalman filter (EnKF) methodology (Peters-Lidard et al., 2011; Xu et al., 2011a, 2011b, 2015a, 2018a; Bateni and Entekhabi, 2012b; Carrera et al., 2015; Xia et al., 2014a, 2014b). The fifth group assimilates sequences of LST measurements into the variational data assimilation (VDA) frameworks to estimate surface heat fluxes (Castelli et al., 1999; Boni et al., 2001; Caparrini et al., 2003, 2004a, 2004b; Crow and Kustas, 2005; Qin et al., 2007; Sini et al., 2008; Bateni and Liang, 2012; Bateni et al., 2013a; Xu et al., 2015b, 2016; Abdolghafoorian et al., 2017).

High temporal resolution LST data from geostationary satellites have been successfully assimilated in the VDA approaches to estimate turbulent heat fluxes (Sini et al., 2008; Bateni et al., 2013b, 2014; Xu et al., 2014). Geostationary satellites can capture the diurnal cycle of LST, and therefore significantly advance the ability of VDA approaches. However, they have relatively low spatial resolution and their coverage mainly focuses on low- and mid-latitudes (Zhang et al., 2014). In contrast, LST data from polar orbiting satellites have high spatial resolution as well as global coverage. Thus, it is a significant achievement if turbulent heat fluxes can be estimated by assimilating low temporal resolution LSTs from polar orbiting satellites.

In this study, the Moderate Resolution Imaging Spectroradiometer (MODIS) LST product (from Aqua and Terra platforms) with 1 km × 1 km spatial resolution and 2-revisit during daytime are assimilated in the VDA assimilation of Bateni et al. (2013a). The unknown parameters of the VDA approach are the neutral bulk heat transfer coefficient ( $C_{HN}$ ) and evaporative fraction (EF).  $C_{HN}$  scales the sum of turbulent heat fluxes (H + LE), and EF scales their partitioning (i.e., EF = LE/(H + LE)). An expression is proposed to parameterize EF in terms of LAI or apparent thermal inertia (ATI) (Wang et al., 2006; Yao et al., 2013; Zhou and Wang, 2016). The a priori EF estimate from the proposed expression is used as an initial guess in the VDA approach. The VDA system finds the optimal values of  $C_{HN}$  and EF (a posteriori EF estimate) by minimizing the difference between measured and estimated LST. The VDA approach is tested in the Heihe River Basin (HRB) (located in northwestern China) under a variety of vegetative and hydrological conditions. The turbulent heat fluxes measurements from the large-aperture scintillometer (LAS) at three sites (Arou, Daman, and Sidaoqiao) in the HRB are used to validate the VDA estimates. Moreover, a number of numerical sensitivity tests are conducted to evaluate the effect of LST temporal sampling on the turbulent heat fluxes esti-

This paper is organized as follows. Section 2 introduces the methodology including the heat diffusion equation, combined- and dual-source surface energy balance equations, EF parameterization scheme, and adjoint state formulation. Section 3 explains the study area and data. Section 4 presents the results and discussions, including the effect of LST temporal sampling on the H and LE estimates. Finally, Section 5 reports the conclusions.

#### 2. Methodology

## 2.1. Heat diffusion equation

The transport of heat through the soil column is governed by the thermal diffusion equation,

$$c\frac{\partial T(z,t)}{\partial t} = K \frac{\partial^2 T(z,t)}{\partial z^2} \tag{1}$$

where T(z,t) is the soil temperature at depth z and time t, and K and c are the soil heat conductivity (W m<sup>-1</sup> K<sup>-1</sup>) and heat capacity (Jm<sup>-3</sup> K<sup>-1</sup>), respectively (de Vries, 1963; Fourier, 1822). The heat diffusion equation is solved by specifying the boundary conditions at the top and bottom of the soil column. The boundary condition at the top of soil column is obtained by using the surface forcing equation -KdT(z=0,t)/dz=G(z=0,t), where G(z=0,t) is the ground heat flux at the land surface at time t (thereafter shown as G). The ground heat flux is assumed to be zero at the bottom boundary of soil column. At the bottom boundary, a Neumann boundary condition is implemented as,

$$dT(l,t)/dz = 0 (2)$$

where l is the depth of bottom boundary. According to Hu and Islam (1995), soil temperature at the depth of 0.3–0.5 m is almost invariant over a daily time scale. Hence, l=0.5 m is used in this study.

#### 2.2. Surface energy balance (SEB)

## 2.2.1. Combined-source SEB scheme

The combined-source (CS) SEB model considers soil and vegetation as a single energy source and can be written as (Bastiaanssen et al., 1998a; Su, 2002),

$$R_N = H + LE + G \tag{3}$$

where H and LE are the sensible and latent heat fluxes (W m<sup>-2</sup>),  $R_N$  is the net radiation (W m<sup>-2</sup>), and G is the ground heat flux (W m<sup>-2</sup>).  $R_N$  can be defined as,

$$R_N = (1 - \alpha)R_S^{\downarrow} + R_L^{\downarrow} - \varepsilon \sigma T^4 \tag{4}$$

where  $\alpha$  is the surface albedo (–), and  $R_S^{\downarrow}$  and  $R_L^{\downarrow}$  are the incoming shortwave and longwave radiation (Wm $^{-2}$ ), respectively.  $\varepsilon$  is the surface emissivity (–),  $\sigma$  is the Stefan-Boltzmann constant (5.67  $\times$  10 $^{-8}$  Wm $^{-2}$  K $^{-4}$ ), and T is the land surface temperature (K).

The sensible heat flux is given by,

$$H = \rho c_p C_H U (T - T_a) \tag{5}$$

where  $\rho$  is the air density (kg m<sup>-3</sup>),  $c_p$  is the air heat capacity (1012 Jkg<sup>-1</sup> K<sup>-1</sup>), and U and  $T_a$  are the reference-height wind speed (m s<sup>-1</sup>) and air temperature (K), respectively.  $C_H$  is the heat transfer coefficient (-), which can be written as the product of the heat transfer coefficient under neutral atmospheric condition ( $C_{HN}$ ) and the atmospheric stability correction function (f(Ri)), i.e.,  $C_H = C_{HN}f(Ri)$ , where Ri is the Richardson number.

Herein, the atmospheric correction function proposed by Caparrini et al. (2003) is used because it performed well in previous studies (Crow and Kustas, 2005; Sini et al., 2008; Bateni and Liang, 2012; Bateni et al., 2013a, 2013b, 2014; Xu et al., 2014, 2016; Abdolghafoorian et al., 2017).  $C_{HN}$  constitutes the first unknown parameter of the CS VDA model. It mainly depends on the characteristics of the landscape, and is set to be invariant in each monthly (30-day) period (Caparrini et al., 2004a, 2004b).

The second unknown parameter of the CS SEB model is EF. Crago (1996) and Gentine et al. (2007) showed that EF is almost constant for daytime hours on days without precipitation. In this study, EF is assumed to be constant during the daytime assimilation window (09:00–18:00 LT) for each day so that latent heat flux can then be

estimated by,

$$LE = \frac{EF}{1 - EF}H$$
(6)

Finally, G is calculated as the residual of the SEB equation (i.e.,  $G = R_N - H - LE$ ).

## 2.2.2. Dual-source SEB scheme

The dual-source (DS) SEB model considers vegetation and soil as different sources of energy, and is able to simulate soil-canopy interaction (Kustas et al., 1996; Kustas and Norman, 1999).

The SEB equations for the soil and canopy can be written as,

$$R_{NS} = H_S + LE_S + G \tag{7a}$$

$$R_{NC} = H_C + LE_C \tag{7b}$$

where  $H_S$ , LE<sub>S</sub>, and  $R_{NS}$  are the sensible heat flux, latent heat flux, and net radiation for the soil, respectively.  $H_C$ , LE<sub>C</sub>, and  $R_{NC}$  are the sensible heat flux, latent heat flux, and net radiation for the canopy, respectively.

Net radiation for soil  $(R_{NS})$  and canopy  $(R_{NC})$  are estimated by establishing a balance between the longwave and shortwave radiation for each component,

$$R_{NS} = (1 - \alpha_S)R_S^{\downarrow} + R_L^{\downarrow} - \varepsilon_S \sigma T_S^4$$
 (8a)

$$R_{NC} = (1 - \alpha_C)R_S^{\downarrow} + R_L^{\downarrow} - \varepsilon_C \sigma T_C^4$$
(8b)

where  $\alpha_c$  and  $\alpha_s$  are the surface albedo for the canopy and soil, and  $\varepsilon_c$  and  $\varepsilon_s$  are the canopy and soil emissivity. The total net radiation ( $R_N$ ) is given by the weighted average of net radiation from the canopy and soil,

$$R_N = f_c R_{NC} + (1 - f_c) R_{NS}$$
(9)

where  $f_c$  is the vegetation cover fraction and can be obtained from LAI by (Norman et al., 1995; Anderson et al., 1997),

$$f_c = 1 - \exp(-0.5\text{LAI}) \tag{10}$$

The sensible heat fluxes can be represented by a conductance network that includes nodes at the soil, the canopy leaves, the within canopy air, and air above the canopy (Caparrini et al., 2004a, 2004b; Bateni and Liang, 2012). The network is characterized by the turbulent heat transfer coefficients  $C_{HS}$  (for heat transfer from soil to air within the canopy) and  $C_{HC}$  (for heat transfer from leaves to air within the canopy).

The sensible heat fluxes for soil  $(H_S)$  and canopy  $(H_C)$  are given by,

$$H_S = \rho C_P C_{HS} U_W (T_S - T_W) \tag{11a}$$

$$H_C = \rho C_P C_{HC} U_W (T_C - T_W) \tag{11b}$$

where  $T_S$  and  $T_C$  are the soil and canopy temperatures, and  $U_W$  and  $T_W$  are the wind speed and air temperature within the canopy. To reduce the unknown parameters of the DS VDA model,  $C_{HS}$  and  $C_{HC}$  are related to  $C_{HN}$  (Bateni and Liang, 2012). Equations for the calculation of  $T_S$ ,  $T_C$ , and  $T_W$  can be found in Bateni and Liang (2012).

The total sensible heat flux (*H*) is given by the weighted average of sensible heat fluxes from the canopy and soil,

$$H = f_c H_C + (1 - f_c) H_S \tag{12}$$

Other unknown parameters of the DS VDA model are the soil and canopy evaporative fraction ( $EF_S$  and  $EF_C$ ). The LST is calculated with a composite of the soil and canopy temperatures as (Anderson et al., 1997),

$$T = [f_c T_C^4 + (1 - f_c) T_S^4]^{0.25}$$
(13)

#### 2.3. Parameterization of evaporative fraction

The CS VDA approach begins with an initial value of EF (a priori EF estimate), and improves it via assimilation of LST data. Dirmeyer et al. (2000) and Lu et al. (2017) parametrized EF in terms of soil wetness index (SWI) by using the Arctan function. Sini et al. (2008) characterized EF in terms of antecedent precipitation index (API) (as an indicator of soil moisture) by the Arctan function. Following these studies, we formulated EF in terms of environmental index ( $\tau$ ) using the following expression:

$$EF = EF_{min} + \frac{2(EF_{max} - EF_{min})}{\pi} Arctan(\varphi\tau)$$
(14)

where  $EF_{max}$  and  $EF_{min}$  are the maximum and minimum EF values for a specific land cover type (e.g., cropland, forest, grassland, barren land, etc.),  $\varphi$  is the calibration coefficient, and  $\tau$  is the environmental index. The magnitudes of  $EF_{max}$ ,  $EF_{min}$ , and  $\varphi$  for different land cover types over the HRB are given in Section 4.1.

EF is affected mainly by soil moisture and LAI (Dirmeyer et al., 2000; Wang et al., 2006; Bateni et al., 2013a; Zhou and Wang, 2016). Over the bare soil, EF is controlled mainly by soil moisture (Dirmeyer et al., 2000). The high spatial resolution (1 km) soil moisture is unavailable over the HRB, and therefore ATI is used as an indicator of soil moisture (Verstraeten et al., 2006; Van doninck et al., 2011; Qin et al., 2013). In this study, ATI is used to parameterize  $\tau$  over the barren land (Eq. (15a)). Over the vegetated areas (cropland, grassland, and forest), LAI is used to estimate  $\tau$  (Eq. (15b)).

$$\tau = \frac{ATI - ATI_{min}}{ATI_{max} - ATI_{min}} \text{ For barren land}$$
 (15a)

$$\tau = \frac{LAI - LAI_{min}}{LAI_{max} - LAI_{min}} \mbox{ For vegetated land} \eqno(15b)$$

where  ${\rm ATI}_{\rm max}$  and  ${\rm ATI}_{\rm min}$  are the maximum and minimum of ATI, respectively.  ${\rm LAI}_{\rm max}$  and  ${\rm LAI}_{\rm min}$  are the maximum and minimum of LAI, respectively.

In this study,  $\tau$  is computed on a daily basis from Eqs. (15a) and (15b). Then, it is substituted in Eq. (14) to calculate EF. The a priori EF estimate from Eq. (14) is used as an initial guess in the CS VDA approach to find a *posterior* (optimal) EF value. It is also used as an initial guess for EF<sub>S</sub> and EF<sub>C</sub> in the DS VDA system.

ATI is calculated by (Short and Stuart Jr., 1982),

$$ATI = C\frac{1-\alpha}{A} \tag{16}$$

where C is the solar correction factor (-), A is the amplitude of diurnal temperature cycle (K), and  $\alpha$  is the surface albedo (-).

Solar correction factor (C) can be estimated from,

$$C = \sin \phi \sin \delta (1 - \tan^2 \phi \tan^2 \delta)^{\frac{1}{2}} + \cos \phi \cos \delta \arccos(-\tan \phi \tan \delta)$$
 (17)

where  $\phi$  is the latitude (rad) of the Earth and  $\delta$  is the solar declination (rad) of the Earth, which can be calculated from,

$$\delta = 0.006918 - 0.399912\cos(\Gamma) + 0.070257\sin(\Gamma) - 0.0067587\cos(2\Gamma) + 0.000907\sin(2\Gamma) - 0.002697\cos(3\Gamma) + 0.00148\sin(3\Gamma)$$
 (18)

where  $\Gamma$  is the day angle (rad), which is computed by  $\Gamma = 2\pi(n_d-1)/365.25$ , and  $n_d$  is the day number (-).

The diurnal temperature cycle is approximated by a sinusoidal curve as follows (Van doninck et al., 2011),

$$T(t) = \overline{T} + \frac{A}{2}\cos(\omega t - \psi) \tag{19}$$

where T(t) is the surface temperature at time t (K),  $\overline{T}$  is the daily mean surface temperature (K),  $\omega$  is the angular velocity of Earth's rotation (rad/s), and  $\psi$  is the phase angle (rad), which can be calculated from

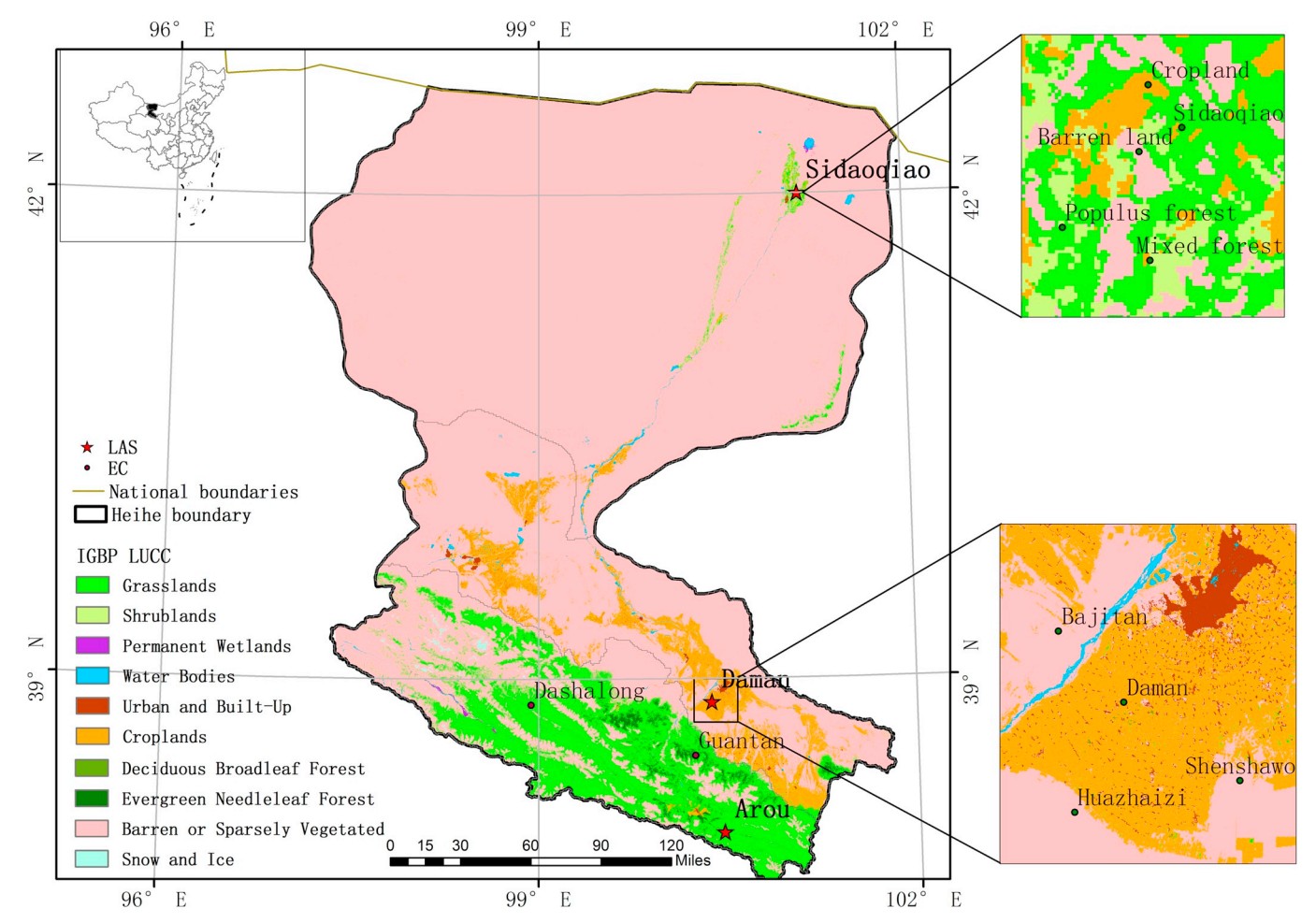


Fig. 1. The land cover map over the HRB.

Van doninck et al. (2011). A and  $\overline{T}$  can be computed in each pixel for each day by the following equations,

$$A = \frac{2(n\sum_{i=1}^{n}\cos(\omega t_{i} - \psi)T(t_{i}) - \sum_{i=1}^{n}\cos(\omega t_{i} - \psi)\sum_{i=1}^{n}T(t_{i}))}{n\sum_{i=1}^{n}\cos^{2}(\omega t_{i} - \psi) - (\sum_{i=1}^{n}\cos(\omega t_{i} - \psi))^{2}}$$
(20)

$$\overline{T} = \frac{\sum_{i=1}^{n} T_i - \frac{A}{2} \sum_{i=1}^{n} \cos(\omega t_i - \psi)}{n}$$
(21)

where n is the number of LST observations in each day (i = 1, 2, ..., n). Van doninck et al. (2011) recommended that the day/night LST pairs be

used in Eqs. (20) and (21) when only two LST observations are available.

## 2.4. Adjoint state formulation

 $C_{HN}$  and EF are the two key unknown parameters of the CS VDA approach. The VDA approach finds the optimum values of the unknown parameters (i.e.,  $C_{HN}$  and EF) by minimizing the difference between the observed and estimated LST. The cost function (J) for the CS VDA model can be written as,

Table 1
List of eddy covariance (EC)/automatic weather station (AWS) observation sites over the HRB.

EC/AWS sites	Observation period	IGBP land cover	Longitude (E)	Latitude (N)	Elevation (m)	EBR
Arou	2012.12-2015.12	Grassland	100.46	38.04	3033	0.84
Dashalong	2013.8-2015.12	Grassland	98.94	38.84	3739	0.83
Daman	2012.9-2015.12	Cropland	100.37	38.85	1556	0.92
Cropland	2013.7-2015.10	Cropland	101.13	42.00	875	0.91
Guantan	2008.1-2012.3	Evergreen needleleaf forest	100.25	38.53	2835	0.89
Populus euphratica	2013.7-2015.12	Deciduous broadleaf forest	101.12	41.99	876	0.87
Mixed forest	2013.7-2015.12	Mixed forest	101.13	41.99	874	0.82
Sidaogiao	2013.7-2015.12	Shrubland	101.13	42.00	873	0.96
Huazhaizi desert steppe	2012.6-2015.12	Barren/sparsely vegetated	100.31	38.76	1731	0.91
Shenshawo sandy desert	2012.6-2015.4	Barren/sparsely vegetated	100.49	38.78	1694	0.93
Bajitan Gobi	2012.6-2015.4	Barren/sparsely vegetated	100.37	38.85	1556	0.93
Barren land	2013.7-2015.3	Barren/sparsely vegetated	101.13	41.99	878	0.89

Note: EC = eddy covariance, AWS = automatic weather stations, IGBP = International Geosphere-Biosphere Programme, and EBR = energy balance ration for the eddy covariance.

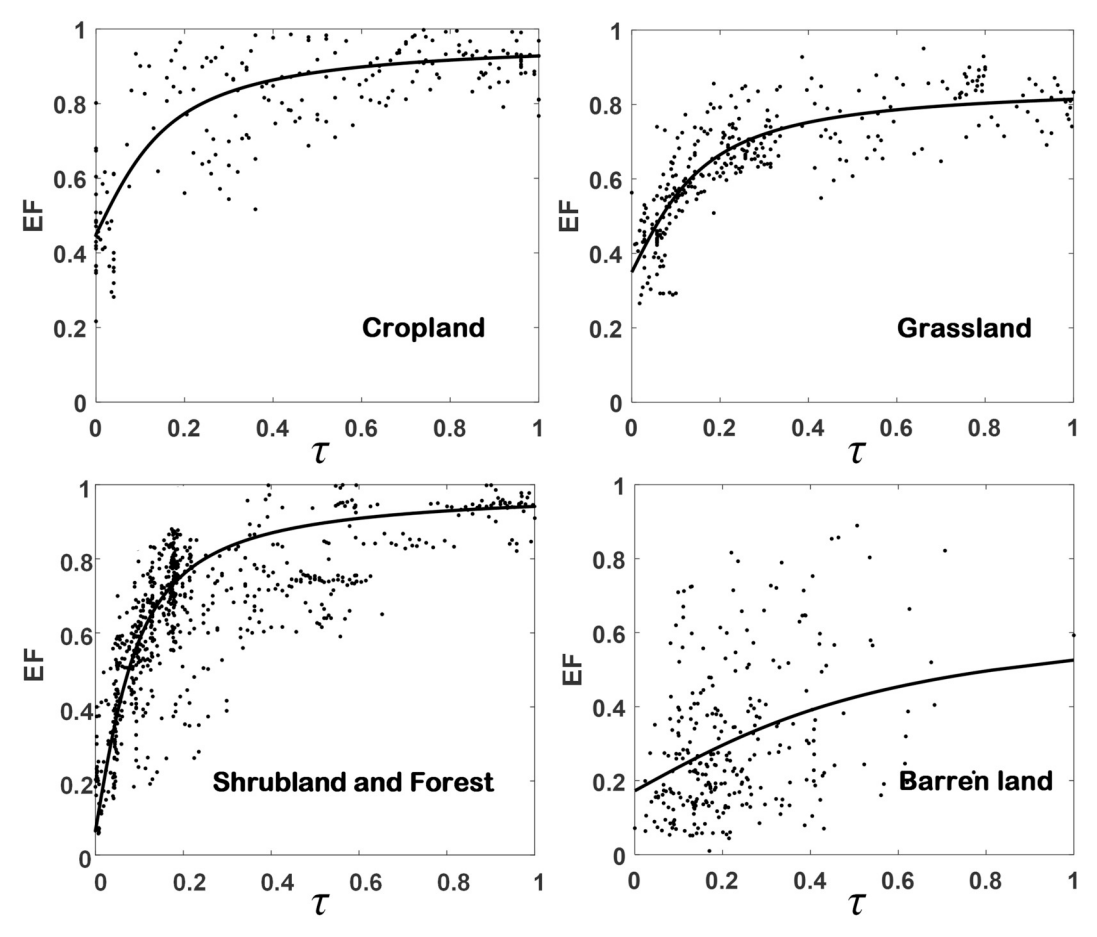


Fig. 2. Measured evaporative fraction (EF) values by the 12 EC systems in the HRB (Table 1) versus environmental index ( $\tau$ ) for the cropland, grassland, forest, and barren land.

**Table 2** Estimated  $\varphi$ ,  $\text{EF}_{\min}$ , and  $\text{EF}_{\max}$  values for each land cover type via the least-square approach.

Land cover type	φ	EF <sub>min</sub>	EF <sub>max</sub>
Forest	13	0.06	0.98
Cropland	7	0.45	0.96
Grassland	7	0.35	0.86
Barren land	2	0.17	0.67

Note:  $\varphi$  is the calibration coefficient (slope factor), and  $\mathrm{EF}_{\mathrm{min}}$  and  $\mathrm{EF}_{\mathrm{max}}$  are the minimum and maximum evaporative fraction over each land cover type.

$$J(T, R, EF, \lambda) = \sum_{i=1}^{N} \int_{t_0}^{t_1} [T_{OBS,i}(t) - T_i(t)]^T K_T^{-1} [T_{OBS,i}(t) - T_i(t)] dt$$

$$+ (R - R')^T K_R^{-1} (R - R') + \sum_{i=1}^{N} (EF_i - EF_i')^T K_{EF}^{-1} (EF_i - EF_i')$$

$$+ 2 \sum_{i=1}^{N} \int_{t_0}^{t_1} \int_{0}^{l} \lambda_i(z, t) \left[ \frac{\partial T_i(z, t)}{\partial t} - D \frac{\partial^2 T_i(z, t)}{\partial z^2} \right] dz dt$$
(22)

The first term on the right-hand side measures the difference between the observed LST from MODIS ( $T_{OBS}$ ) and the predicted LST from the heat diffusion equation (T). The second and third terms represent the misfit between R and EF estimates and their priori values, respectively.  $C_{HN}$  is related to R via  $C_{HN} = \exp(R)$  to make it strictly positive. The initial value of EF can be obtained from Eq. (14). The last term is the heat diffusion equation, which is adjoined to the model by the Lagrange multiplier  $\lambda$ . D = K/C is the heat diffusion coefficient.  $K_T^{-1}$ ,  $K_R^{-1}$ ,

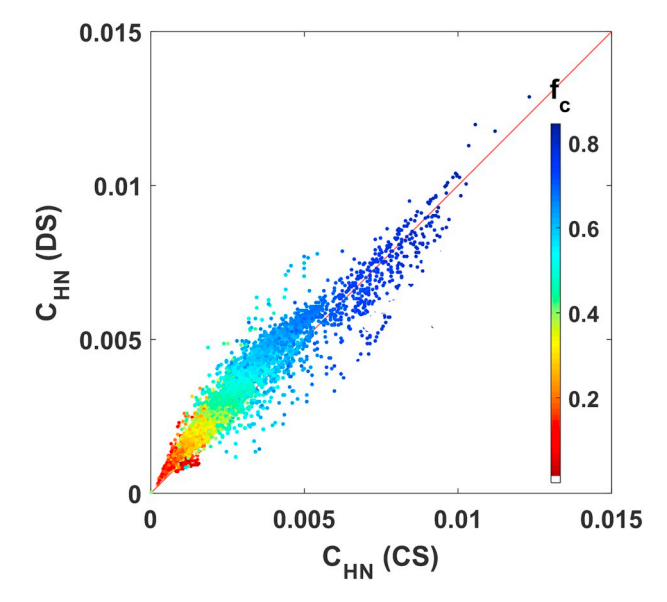


**Fig. 3.** Comparing the  $C_{HN}$  estimates from the CS and DS VDA approaches. The color of the points is mapped to the value of  $f_c$ .

and  $K_{EF}^{-1}$  are numerical constants, which determine the weight of each term in the cost equation and control the convergence rate of the VDA system. Following Bateni et al. (2013a),  $K_T^{-1}$ ,  $K_R^{-1}$ , and  $K_{EF}^{-1}$  are set to 0.01 K<sup>-2</sup>, 1000, and 1000, respectively.

Similarly, in the DS VDA approach,  $C_{HN}$ , EF<sub>C</sub>, and EF<sub>S</sub> are found by minimizing the difference between the LST observations and

estimations. The cost function for the DS VDA approach is defined as,

$$J(T, R, EF_C, EF_S, \lambda) = \sum_{i=1}^{N} \int_{t_0}^{t_1} [T_{OBS,i}(t) - T_i(t)]^T K_T^{-1} [T_{OBS,i}(t) - T_i(t)] dt$$

$$+ (R - R')^T K_R^{-1} (R - R') + \sum_{i=1}^{N} (EF_{s,i} - EF_{s,i}')^T K_{EF_s}^{-1} (EF_{s,i} - EF_{s,i}')$$

$$+ \sum_{i=1}^{N} (EF_{c,i} - EF_{c,i}')^T K_{EF_c}^{-1} (EF_{c,i} - EF_{c,i}')$$

$$+ 2 \sum_{i=1}^{N} \int_{t_0}^{t_1} \int_{0}^{t} \lambda_i(z, t) \left[ \frac{\partial T_{s,i}(z, t)}{\partial t} - D \frac{\partial^2 T_{s,i}(z, t)}{\partial z^2} \right] dz dt$$

$$(23)$$

The first term on the right-hand side measures the difference between the observed LST from MODIS ( $T_{OBS}$ ) and the estimated LST from Eq. (13). The second term is similar to that in the CS VDA system. The third and fourth terms measure the difference between the soil and canopy evaporative fraction estimates and their priori values, respectively. In this study, the initial values of EF<sub>S</sub> and EF<sub>C</sub> are set to the EF value obtained from Eq. (14).  $K_T^{-1}$ ,  $K_R^{-1}$ ,  $K_{EF_s}^{-1}$ , and  $K_{EF_c}^{-1}$  are equal to  $0.01 \, \mathrm{K}^{-2}$ , 1000, 1000, and 1000, respectively (Bateni and Liang, 2012).

The optimum values of the unknown parameters of the CS VDA approach (i.e.,  $C_{HN}$  and EF) are found by minimizing the cost function presented in Eq. (22). Similarly, the optimum values of the unknown

parameters of the DS VDA system (i.e.,  $C_{HN}$ , EF<sub>S</sub>, and EF<sub>C</sub>) are found by minimizing the cost function shown in Eq. (23).

To minimize the cost functions (i.e., Eqs. (22) and (23)), their first variations (i.e.,  $\delta J=0$ ) should be set to zero. In Eq. (22), we need to minimize the first three terms and satisfy the heat diffusion constraint simultaneously. Analogously, in Eq. (23), the first four terms should be minimized, and the heat diffusion constraint should be fulfilled. Imposing  $\delta J=0$  leads to a number of equations (the so-called Euler-Lagrange equations), which should be solved simultaneously through an iterative procedure on a monthly basis. These Euler-Lagrange equations can be found in Bateni et al. (2013a) and Xu et al. (2014).

#### 3. Study domain and data

The HRB is the second-largest inland river basin in northwest China. It runs from south of the Qilian Mountains, through the central Hexi corridor to the Northern League grassland, covering an area of approximately  $1.43 \times 10^6 \, \mathrm{km^2}$ . The upstream of HRB has an elevation of  $1000-5000 \, \mathrm{m}$ , a large temperature variation, and various vegetation types. Fig. 1 shows the location of the HRB and its main land covers. The land covers are mainly grassland/forest, barren-land/cropland, and barren-land/forest in the upstream, midstream, and downstream of the HRB, respectively (Zhong et al., 2014, 2015). The turbulent heat fluxes measurements by the eddy covariance (EC) and LAS techniques are available from "Heihe Watershed Allied Telemetry Experimental

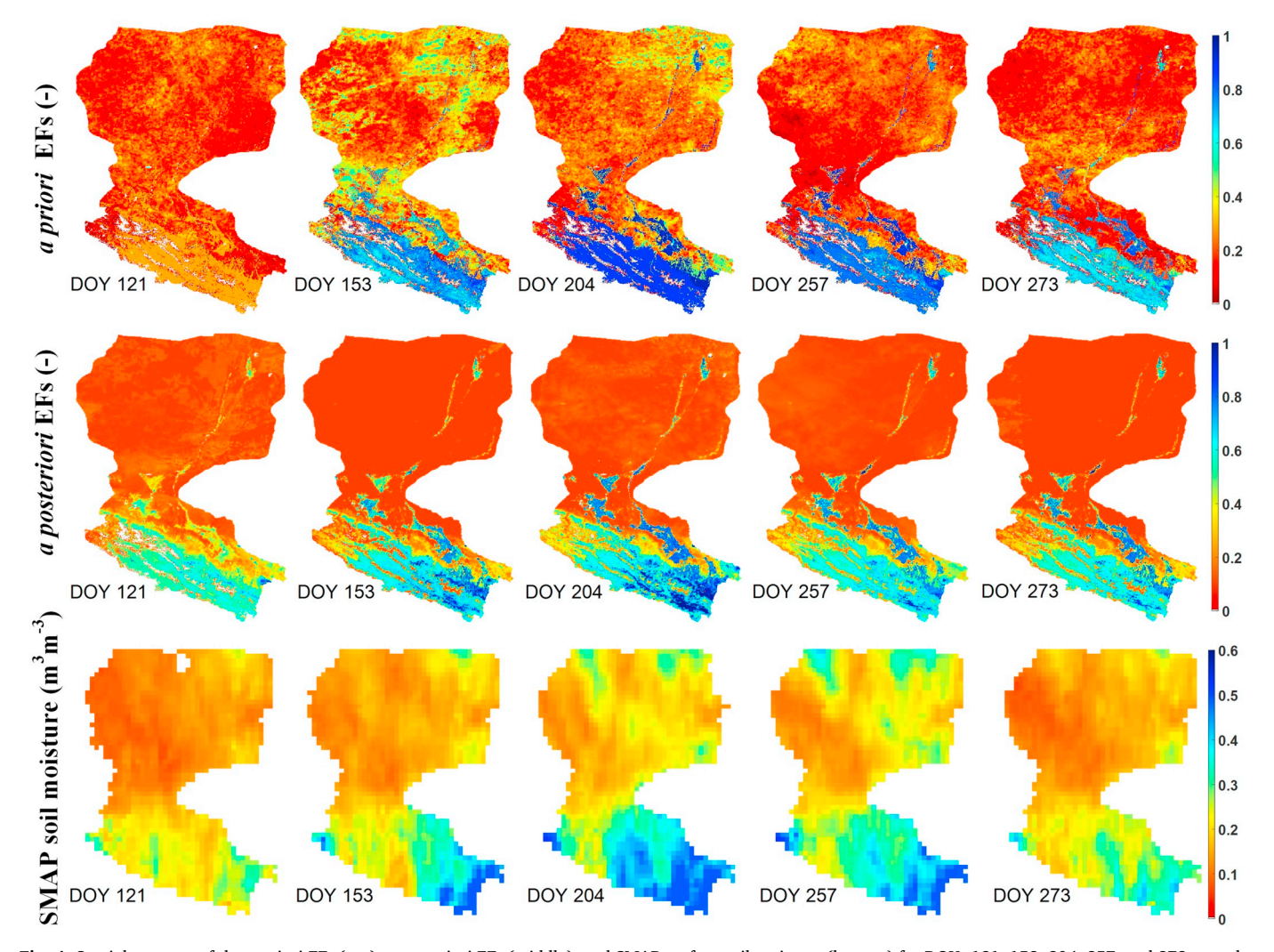


Fig. 4. Spatial patterns of the a priori EF<sub>S</sub> (top), a posteriori EF<sub>S</sub> (middle), and SMAP surface soil moisture (bottom) for DOYs 121, 153, 204, 257, and 273 over the HRB.

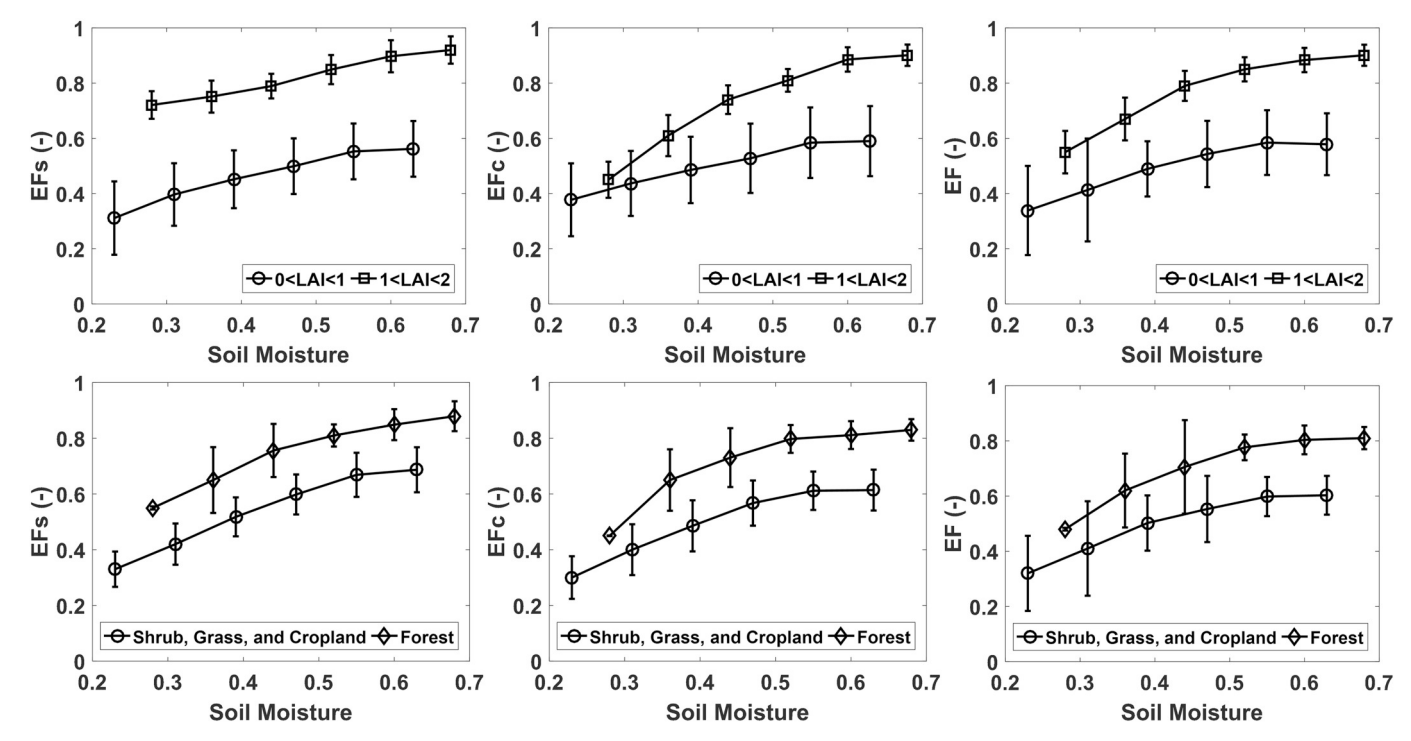


Fig. 5. Plot of estimated soil evaporative fraction (EFs), canopy evaporative fraction (EFc), and evaporative fraction (EF) values versus SMAP soil moisture for two LAI classes (i.e., LAI < 1 and 1 < LAI < 2) (top) and two plant functional types (bottom) with one standard deviation variability in each soil moisture bin.

Research" (HiWATER) launched in the HRB since 2012 (Li et al., 2013; Liu et al., 2011; Xu et al., 2018b). The satellite and aerial remote sensing data, in conjunction with ground-based measurements during this experiment, significantly improve the observability of ecology and hydrology in the HRB. The experiment data can be downloaded freely at the Heihe Data Archive (http://www.heihedata.org/).

The hourly sensible and latent heat fluxes are measured by the EC systems at 12 sites in the HRB (see Table 1). Sensible heat flux is also measured by the LAS instrument in Arou (upstream), Daman (midstream), and Sidaoqiao (downstream) sites (Fig. 1). Latent heat flux (LE) in these sites is obtained as the residual of the SEB equation (LE =  $R_N - G - H$ ) during the vegetation growing season. The net radiation is measured by a four-component radiometer, and the ground heat flux is obtained by a ground heat flux plate. The energy balance ratio of sensible and latent heat fluxes from the EC system is also shown in Table 1. The detailed data processing procedure can be found in Li et al. (2018) and Xu et al. (2013).

The hourly micrometeorological data (wind speed, air temperature and humidity, atmospheric pressure, and incoming shortwave and longwave radiation) produced by the Weather Research and Forecasting (WRF) model are used as inputs in the VDA system (Pan et al., 2012). LST observations are obtained from the Moderate Resolution Imaging Spectroradiometer (MODIS) (i.e., MOD11A1 and MYD11A1) with the spatial resolution of 1 km and frequency of 2 times per day (https://ladsweb.nascom.nasa.gov/search/). Albedo and LAI data are downloaded from the Global Land Surface Satellite (GLASS) product (Xiao et al., 2014, 2016) (http://glass-product.bnu.edu.cn/). Soil moisture data are obtained from the Soil Moisture Active Passive (SMAP) product, with the spatial resolution of 9 km × 9 km (https://search.earthdata.nasa.gov/). The SMAP soil moisture product is not used as input in the VDA approach. It is utilized as an independent dataset to validate the EFs estimates.

Following de Vries (1963) and Chen (2008), the soil heat conductivity (K) and heat capacity (c) are calculated from the soil type and moisture. The soil type is found from the HRB Digital Soil Mapping product (Song et al., 2016b).

#### 4. Results and discussions

#### 4.1. EF values for different land covers

Fig. 2 shows EF values from all the EC flux towers versus the environmental index ( $\tau$ ) for four land cover types: cropland, grassland, forest, and barren land. The cropland is mainly covered by seeded corns. The grassland consists mainly of alpine meadow. The forest is a mixture of deciduous broadleaf forest, evergreen coniferous forests, and shrub. The barren land consists of barren or sparsely vegetated lands. A curve is fitted to the data points in each scatterplot in Fig. 2. The EF observations (calculated from the EC systems) are collected mainly in the growing season (May–September) from 2008 to 2015. Because of the energy imbalance of the EC systems, the measured turbulent heat fluxes are corrected for closure on a daily basis using the Bowen ratio closure method (Twine et al., 2000).

In the vegetated areas (i.e., cropland, grassland, and forest), EF increases rapidly at low  $\tau$  values and reaches a plateau toward higher  $\tau$  values. Compared to the grassland and cropland, EF increases more rapidly in the forest as  $\tau$  increases. This occurs because forests have stronger roots, and thus can uptake and transpire water from the soil profile more robustly. For each land cover type, the parameters  $\varphi$ , EF<sub>min</sub>, and EF<sub>max</sub> in Eq. (14) are determined by the least-square method (see Table 2).

## 4.2. Neutral bulk heat transfer coefficient

The estimated  $C_{HN}$  values from the CS and DS VDA approaches over the HRB are shown in Fig. 3. The points are color-coded based on their vegetation coverage fraction  $(f_c)$  values. This allows comparing performance of the CS and DS schemes for different canopy densities. The  $C_{HN}$  estimates from both the CS and DS schemes increase with the increase of  $f_c$ . The scatter plots mainly fall around the 1:1 line, and the  $C_{HN}$  values from the DS scheme is slightly larger than those of the CS model. For low values of  $f_c$  ( $f_c$  < 0.2), the land surface is mainly composed of soil and its heterogeneity is low. Hence, the discrepancy of  $C_{HN}$  estimates from the CS and DS VDA methods is negligible. With the

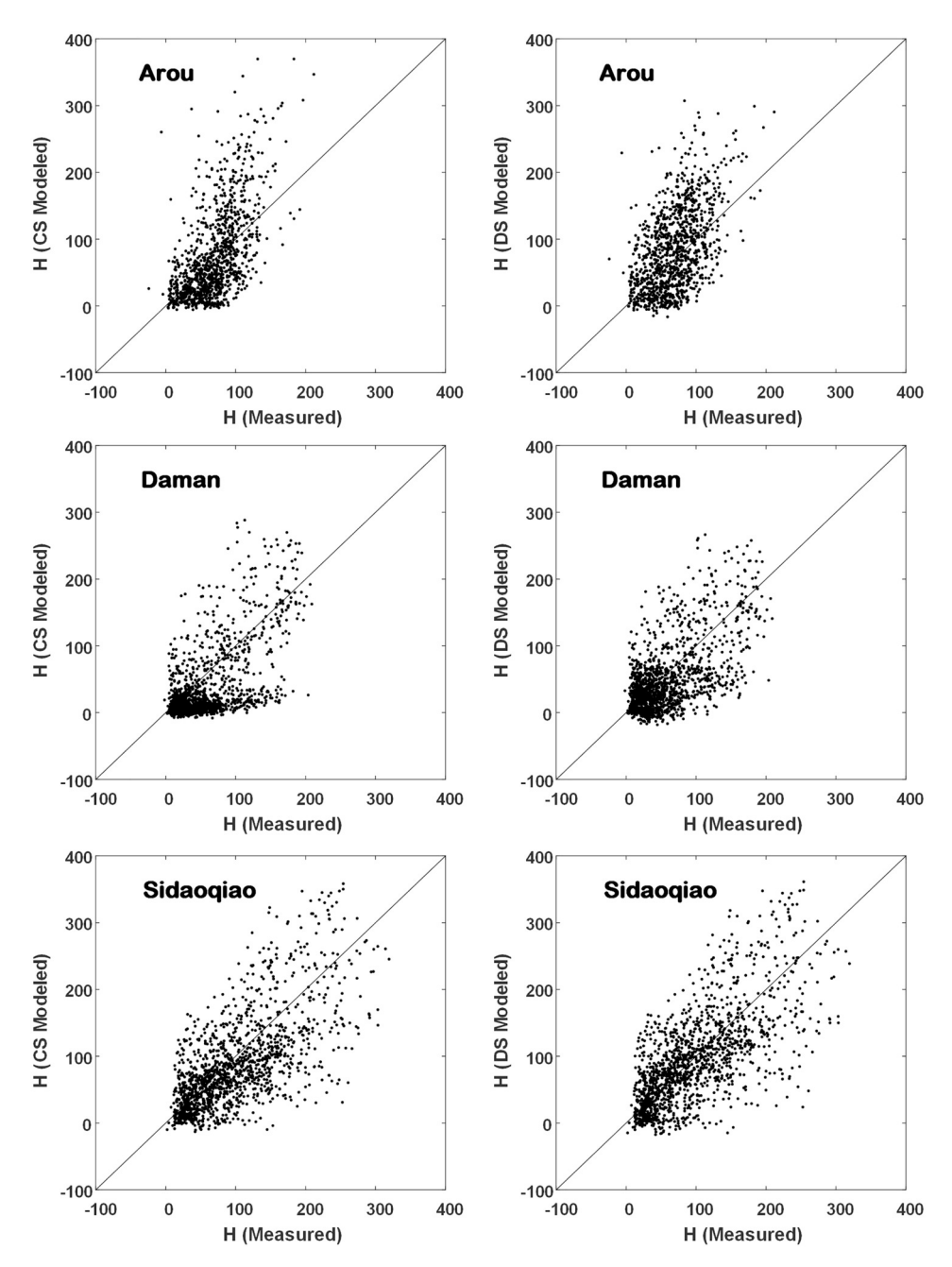


Fig. 6. Scatterplot of hourly sensible heat flux estimates from the CS (left) and DS (right) VDA schemes versus measurements at the Arou, Daman, and Sidaoqiao sites for DOYs 121–273 in 2015.

increase of  $f_c$ , the discrepancy of CS and DS  $C_{HN}$  estimates grows. This difference reaches its maximum when  $f_c$  is around 0.5 where the land surface is heterogeneous. This is because the CS model does not distinguish the difference between the soil and canopy temperatures and treats the LST as a mixed effective temperature for the soil-vegetation media. In contrast, the DS VDA scheme divides the LST into the soil and canopy temperatures and considers the interactions of the soil and canopy. Therefore, the largest difference between the CS and DS  $C_{HN}$  estimates occurs at  $f_c = 0.5$ . When  $f_c$  reaches about 0.8, the surface is mainly composed of canopy and its heterogeneity is reduced. As a result, the discrepancy of the  $C_{HN}$  estimates from the CS and DS schemes is decreased.

Fig. 3 also shows that the  $C_{HN}$  values from the DS VDA scheme are slightly larger than those from the CS VDA scheme. This is due to the different structures of the CS and DS models. The  $C_{HN}$  values from the CS and DS models can be related by,

$$(C_{HN})_{DS} = (C_{HN})_{CS} \frac{T - T_a}{T_W - T_a}$$
 (24)

Within the data assimilation window, the LST (T) is usually larger than the air temperature within the vegetation canopy  $(T_W)$ . This leads to  $(T - T_a) > (T_W - T_a)$ , and the  $C_{HN}$  estimates from the DS VDA scheme should be typically higher than those from the CS VDA scheme.

## 4.3. Evaporative fraction

Soil moisture is the key indicator of soil evaporative fraction (EF<sub>S</sub>) (Dirmeyer et al., 2000; Gentine et al., 2007; Bateni et al., 2013b), and therefore the spatial patterns of EF<sub>S</sub> estimates should be consistent with those of soil moisture. To test the robustness of the DS VDA approach, the a priori (obtained from Eq. (14)) and a posteriori (obtained from the VDA approach) EF<sub>S</sub> maps are compared with the soil moisture data

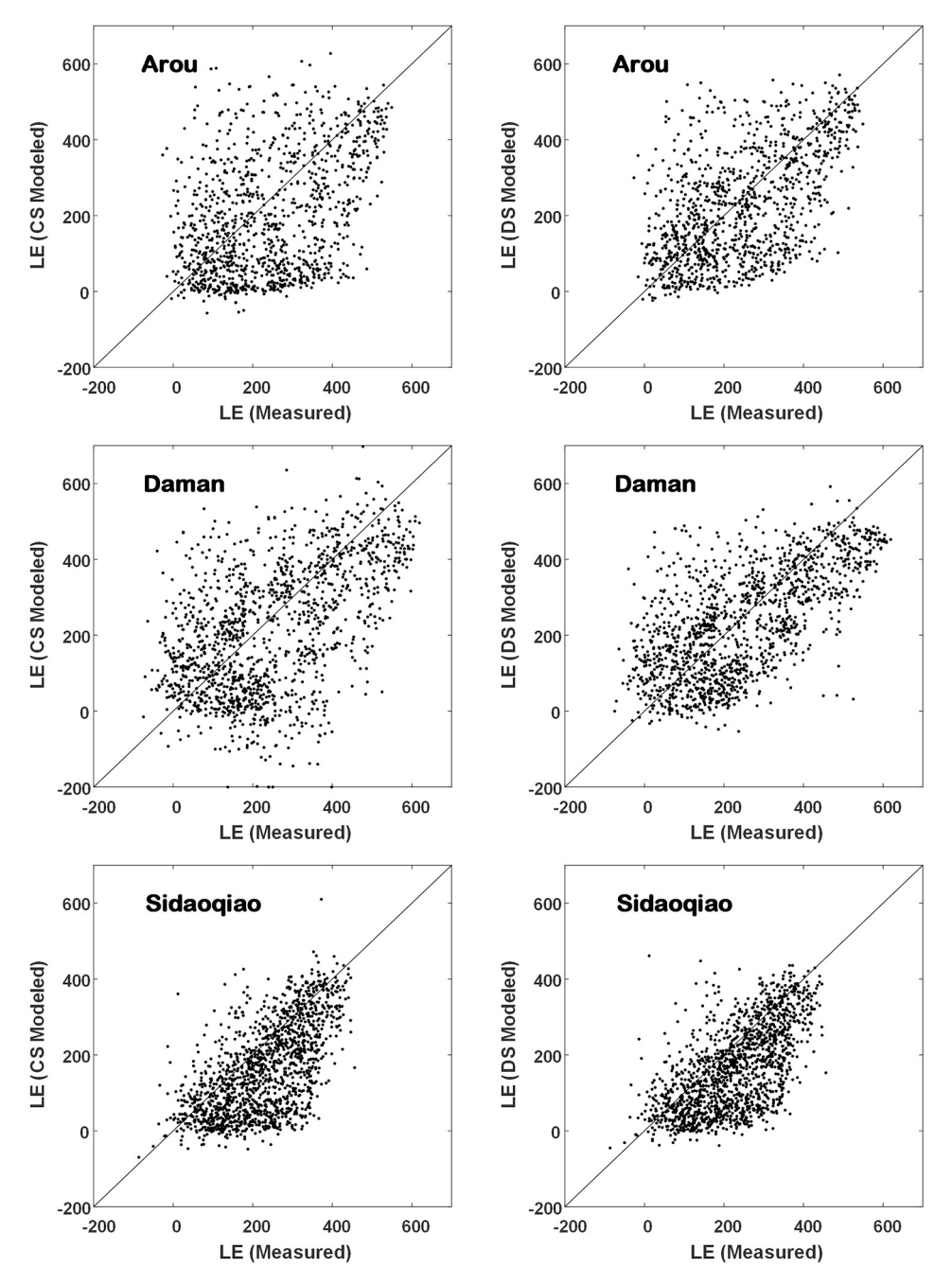


Fig. 7. Scatterplot of hourly latent heat flux estimates from the CS (left) and DS (right) VDA schemes versus measurements at the Arou, Daman, and Sidaoqiao sites for DOYs 121–273 in 2015.

from the SMAP mission. Fig. 4 shows the spatial distribution of a priori (first row) and a posteriori (second row)  $\rm EF_S$  estimates as well as SMAP soil moisture data (third row) over the HRB for Day of Year (DOYs) 121, 153, 204, 257, and 273. As shown, the DS VDA approach improves the  $\rm EF_S$  estimates from Eq. (14) (first row), and patterns in the a posteriori  $\rm EF_S$  estimates (second row) can capture those of soil moisture (third row) more robustly. For example, there is a sharp gradient in soil moisture in the south of the HRB (i.e., soil moisture is high (low) in southeast (southwest) of the HRB) in DOYs 153, 204, and 257. Remarkably, a distinct southwest-southeast gradient is observed in the retrieved  $\rm EF_S$  values from the VDA approach, while the a priori  $\rm EF_S$  estimates are higher southeast of the HRB and show no gradient. Both the  $\rm EF_S$  and SMAP soil moisture maps show a sharp north-south gradient. They are highest upstream of the HRB (in the south) due to the heavy precipitation over the high altitude mountainous areas, but

decrease over midstream and downstream of the HRB because of low precipitation. EFs and soil moisture are higher in midstream than downstream due to relatively larger irrigated oasis areas in the midstream.

Fig. 5 shows variations of EFs, EFc, and EF estimates versus soil moisture for different LAI values. EFs, EFc, and EF estimates increase at low soil moisture and reach a plateau toward higher values of soil moisture. EFc increases mildly for sparser vegetation cover (i.e., LAI < 1), but rises sharply for denser canopy cover (i.e., 1 < LAI < 2). Dense canopies have a strong root uptake potential and can extract moisture from the soil profile more robustly to accelerate the transpiration rate. Unlike EFc, the variation of EFs versus soil moisture is insensitive to the amount of LAI, and EFs estimates have almost the same rate of increase for both LAI classes. EFs values for denser canopy cover (1 < LAI < 2) are higher than those of the sparser canopy cover

**Table 3a** Statistical indices of hourly *H* estimates from the CS and DS open-loop and VDA models at the three experimental sites.

Site	Statistical metric	CS		DS	
		Open-loop	VDA	Open-loop	VDA
Arou	Bias (W m <sup>-2</sup> )	24.31	14.07	19.15	-4.41
	MAPE (%)	43.41	35.30	35.54	26.72
	RMSE (W m $^{-2}$ )	50.61	30.19	45.59	23.14
	$R^2$	0.58	0.66	0.65	0.72
Daman	Bias (W m $^{-2}$ )	28.12	21.89	25.69	10.29
	MAPE (%)	53.33	45.19	50.42	35.64
	RMSE (W m $^{-2}$ )	55.32	39.42	49.55	28.09
	$\mathbb{R}^2$	0.47	0.61	0.51	0.72
Sidaoqiao	Bias (W m $^{-2}$ )	18.98	12.70	15.34	3.22
	MAPE (%)	40.28	33.84	35.61	23.67
	RMSE (W m $^{-2}$ )	60.59	42.72	49.54	38.84
	$\mathbb{R}^2$	0.42	0.67	0.55	0.73
Three-sites-average	Bias (W m $^{-2}$ )	23.80	16.22	20.06	3.03
	MAPE (%)	45.67	38.11	40.52	28.68
	RMSE (W m $^{-2}$ )	55.51	37.44	48.23	30.02
	$R^2$	0.49	0.65	0.57	0.72

Table 3b Statistical indices of hourly LE estimates from the CS and DS open-loop and VDA models at the three experimental sites.

Site	Statistical metric	CS		DS	
		Open-loop	VDA	Open-loop	VDA
Arou	Bias (W m <sup>-2</sup> )	45.32	36.15	40.21	6.75
	MAPE (%)	46.85	35.08	39.54	25.69
	RMSE (W m $^{-2}$ )	150.52	115.85	132.41	84.88
	$\mathbb{R}^2$	0.49	0.59	0.53	0.62
Daman	Bias (W $m^{-2}$ )	61.22	46.69	56.91	22.70
	MAPE (%)	39.54	26.52	50.21	21.57
	RMSE (W m $^{-2}$ )	115.25	84.43	110.25	61.45
	$R^2$	0.49	0.66	0.55	0.75
Sidaoqiao	Bias (W $m^{-2}$ )	95.41	68.01	82.45	61.42
	MAPE (%)	41.25	31.44	40.38	20.48
	RMSE (W m $^{-2}$ )	100.02	82.61	93.51	76.11
	$\mathbb{R}^2$	0.45	0.68	0.53	0.71
Three-sites-average	Bias ( $W m^{-2}$ )	67.32	50.28	59.86	30.29
	MAPE (%)	42.55	31.01	43.38	22.58
	RMSE (W m $^{-2}$ )	121.93	94.30	112.06	74.15
	$R^2$	0.48	0.64	0.54	0.69

(LAI < 1). The denser canopy cover reduces the available energy at the soil surface, causing a reduction in the soil temperature. Reduced soil temperature results in a decrease in the difference between the soil temperature  $(T_S)$  and air temperature  $(T_W)$  within the canopy, ultimately causing a decrease in the soil sensible heat flux. Therefore,  $\ensuremath{\text{EF}_S}$ tends to be higher for dense vegetation cover. Fig. 5 also shows the effect of plant functional type on the EFs-, EFc-, and EF-soil moisture relationship. EFs values for the forest are higher than those of shrub, grass, and cropland because forests typically have a denser vegetation cover than shrub, grass, and cropland. EFC values for the forest increases more sharply than those of shrub, grass, and cropland because the deeper roots of forest can uptake deep soil moisture, leading to a larger transpiration. In contrast, EFS estimates for both of the plant functional types have almost the same rate of increase, and EFs values for the forest are higher than those of shrub, grass, and cropland because forests usually have a denser vegetation cover. As anticipated, EF of forest rises more sharply with soil moisture because of its deeper

## 4.4. Sensible and latent heat fluxes

Fig. 6 compares the hourly sensible heat flux estimates from the CS and DS VDA schemes with the measurements at the Arou, Daman, and

Sidaoqiao sites. Similarly, Fig. 7 shows this comparison for latent heat flux. As indicated, the retrieved sensible and latent heat fluxes from the CS and DS models agree well with the observations, and mainly fall around the 1:1 line. The DS model performs slightly better than the CS model because the DS scheme represents the physics of the problem more robustly than the CS model. The statistics of turbulent heat flux estimates at the three sites are summarized in Tables 3a and 3b. For sensible heat flux, the three-site-averaged bias (RMSEs) from the CS and DS schemes are 16.22 (37.44) and 3.03 (30.02)  $W m^{-2}$ , respectively. For latent heat flux, the three-site-averaged bias (RMSE) is 50.28  $(94.30) \text{ W m}^{-2}$  for the CS model, and 30.29  $(74.15) \text{ W m}^{-2}$  for the DS scheme. The low bias and RMSE values indicate that the CS and DS schemes can accurately estimate turbulent heat fluxes over various vegetative and hydrological conditions. The statistical metrics show that the decomposition of the surface into the vegetation and soil by the DS model improves the turbulent heat fluxes estimates compared to the CS model. As indicated in Tables 3a and 3b, the mean absolute percent errors (MAPEs) of turbulent heat fluxes estimates from the CS and DS models at the Arou site, with higher precipitation and denser vegetation cover (LAI = 2.7), are larger than those at the Sidaoqiao site with lower precipitation and sparser canopy cover (LAI = 0.6). In fact, both the CS and DS VDA approaches perform better in relatively dry and/or slightly vegetated conditions (e.g., Sidaoqiao site). In contrast, performance of the CS and DS VDA approaches degrade in wet and/or densely vegetated conditions (e.g., Arou and Daman sites). In dry and/or slightly vegetated sites, the drying rate is mainly controlled by the land surface state variables (i.e., LST and LAI). In contrast, the drying rate is mainly affected by the atmospheric state variables (i.e., air temperature and specific humidity) in wet and/or densely vegetated sites (Shokri et al., 2008a, 2008b). As a result, the VDA approach (that retrieves the optimum values of  $C_{HN}$  and EF by assimilating LST data) performs better at dry/slightly vegetated sites (Crow and Kustas, 2005; Xu et al., 2014, 2016).

The discrepancies between the model estimates and observations are mainly due to the model physical assumptions (constant soil thermal conductivity (K) and heat capacity (c), daily constant EF, EF<sub>C</sub>, and  $EF_S$ , monthly constant  $C_{HN}$ , and measurement errors), and uncertainties in the model inputs (e.g., atmospheric variables, LST, and LAI). Remotely sensed LST and LAI data contain noise, which adversely affects the performance of the VDA approach. The readers are referred to Xu et al. (2014) for a detailed sensitivity analysis on the impact of uncertainties in LST and LAI on the turbulent heat fluxes estimates from the VDA approach. Moreover, this study uses the radiometric LST provided by the MODIS product in lieu of the aerodynamic LST. However, there is a difference between the radiometric and aerodynamic LSTs, which results in errors in the turbulent heat fluxes estimates (Norman and Becker, 1995; Voogt and Grimmond, 2000). Future studies should examine uncertainties in the H and LE estimates due to assimilating radiometric LST data in the VDA system.

Figs. 6 and 7 also show that LE estimates are more scattered around the 45-degree line compared to H retrievals. This is because the uncertainty of H estimates is due to errors in the  $C_{HN}$  and LST estimates (see Eq. (5)), while the uncertainty of LE estimates is because of errors in the  $C_{HN}$ , EF, and LST estimates (see Eq. (6)). More sources of errors increase the uncertainty of estimated LE values. In addition, H measurements are obtained by the LAS instrument (Liu et al., 2011), while LE observations are obtained as the residual of the SEB equation (i.e., LE =  $R_N - H - G$ ), which may lead to errors in LE observations.

The bias, RMSE, and MAPE of the turbulent heat fluxes estimates from the open-loop and VDA models at the three experimental sites are summarized in Tables 3a and 3b. The open-loop model does not assimilate MODIS LST data. The lower bias, RMSE, and MAPE values from the CS and DS VDA approaches imply that the assimilation of MODIS LST data improves the turbulent heat fluxes estimates. In the CS (DS) VDA scheme, the RMSE of H estimates decreases from 55.51 W m<sup>-2</sup> (48.23 W m<sup>-2</sup>) to 37.44 W m<sup>-2</sup> (30.02 W m<sup>-2</sup>) by assimilating MODIS

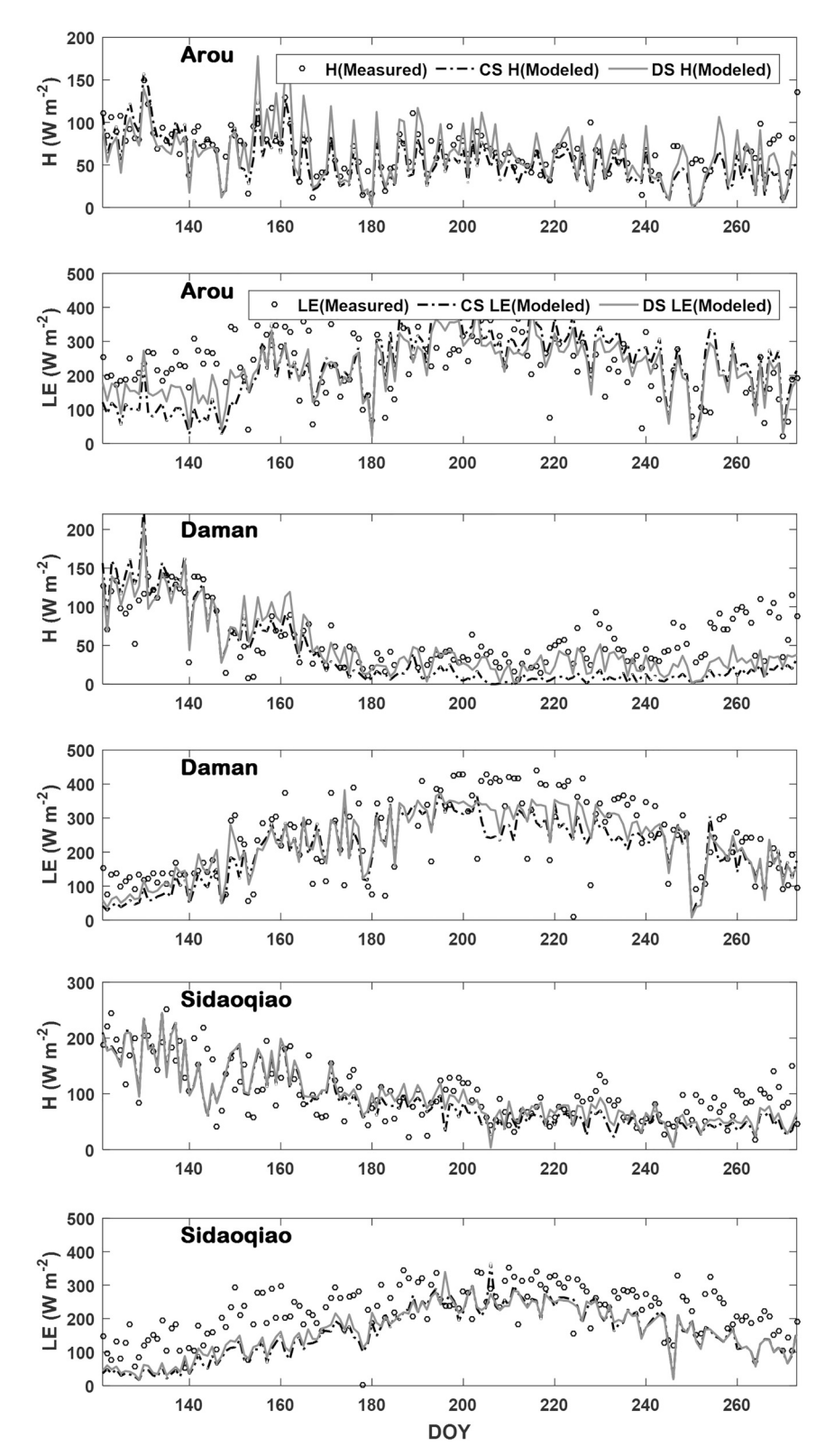


Fig. 8. Time series of daytime-averaged (0900-1800 LT) *H* and LE estimates from the CS (dashed lines) and DS (solid lines) VDA models at the Arou, Daman, and Sidaoqiao sites. *H* and LE observations are shown by open circles.

LST data. Similarly, the RMSEs of LE estimates from the CS and DS models are reduced by 22.66% and 33.83%, by assimilating LST data. Fig. 8 shows the time series of observed and estimated daytime-averaged (0900–1800 LT) *H* and LE over the Arou (grassland), Daman (cropland), and Sidaoqiao (shrub-forest) sites during DOYs 121–273, 2015. As indicated, the CS and DS model estimates are consistent with

the observations in terms of both magnitude and day-to-day dynamics, implying that assimilating MODIS LST data can reliably partition the available energy between the sensible and latent heat fluxes. Results from the DS model are closer to the observations compared to those of the CS model. LE increases rapidly in the early stage of the growing season (DOYs 121–181) and reaches its maximum in mid-July (around

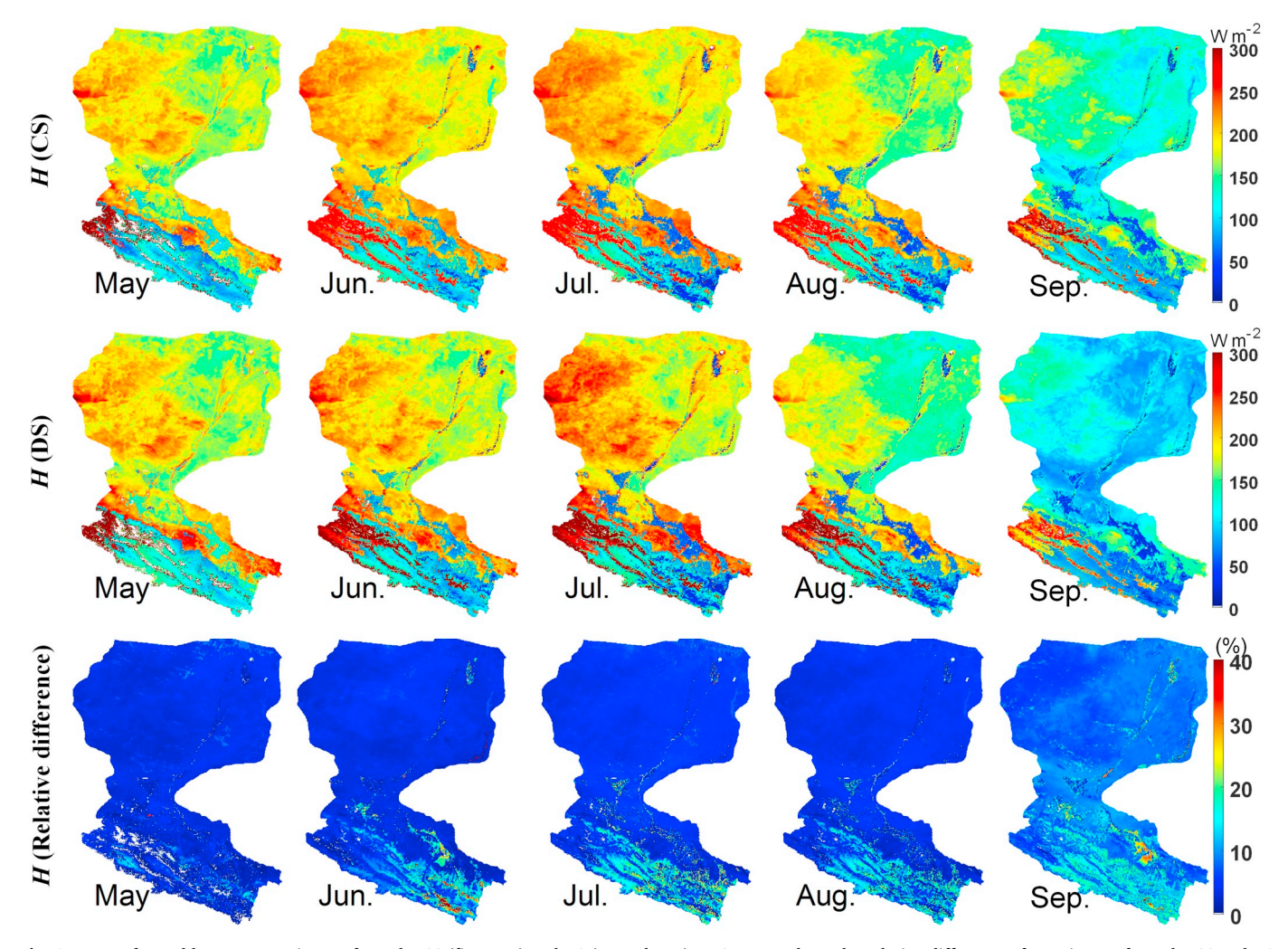


Fig. 9. Maps of monthly mean H estimates from the CS (first row) and DS (second row) VDA approaches. The relative difference of H estimates from the CS and DS models ( $(H_{DS}-H_{CS})/H_{DS} \times 100$ ) is shown in the third row.  $H_{DS}$  and  $H_{CS}$  denote the sensible heat flux estimates from the DS and CS models, respectively.

DOY 200) at the Arou, Daman, and Sidaoqiao sites. Then, the vegetation density and LE gradually reduce. The turbulent heat flux estimates degrade during the wet or densely vegetated periods (e.g., DOYs 180–210 at the Arou site and DOYs 195–240 at the Daman site). At the Daman site, the daytime-averaged latent heat flux measurements increase to approximately  $400\,\mathrm{W\,m^{-2}}$  during the wet period (DOYs 200–220). However, LE estimates cannot reach  $400\,\mathrm{W\,m^{-2}}$  because the upper bounds of EF (in the CS model), and EFs and EFc (in the DS model) are set to 0.99 to avoid numerical instabilities.

Fig. 9 shows the monthly mean H estimates from the CS (first row) and DS (second row) VDA schemes as well as their relative difference (third row) over the HRB during the growing season (May-September). Similarly, Fig. 10 indicates the CS and DS monthly mean LE estimates, and their relative difference. The H (LE) values are higher (lower) in barren areas than grasslands, croplands, and forest. Over the barren regions in the north, H increases from May to July, and decreases from July to September due to the seasonal variation in the incoming solar radiation. LE increases from May to July and then decreases from July to September over the vegetated land covers (i.e., grassland, forest, and cropland), but it is relatively constant over the barren areas due to low precipitation. In the upstream of the HRB, the spatial patterns of retrieved latent heat flux consistently resemble the features in the rainfall and vegetation cover. Regions and periods with higher precipitation and dense vegetation have correspondingly higher LE values. In the midstream of the HRB, the spatial patterns of LE agree well with the oasis areas caused by the crop irrigation. In the north and center of the

HRB (where fc is almost zero), the turbulent heat fluxes estimates from the CS and DS methods have a small relative difference, but the relative difference increases toward the south of the HRB (where fc is mostly non-zero).

Fig. 11 shows the relative difference of H and LE estimates from the CS and DS models for different  $f_c$  values over the HRB. The maximum relative difference occurs for  $f_c$  of  $\sim$ 0.55. When  $f_c$  is  $\sim$ 0.55, the surface heterogeneity reaches its peak, and the CS model cannot describe the physics of the problem as accurately as the DS model. Hence, the difference between the turbulent heat fluxes estimates from the CS and DS models finds its maximum value. When  $f_c$  is  $\sim$ 0.1, the land surface patchiness is low because the land surface is mainly composed of bare soil. Hence, the discrepancy between the results of the CS and DS models has its lowest value, which is mainly due to the different model structures.

Fig. 12 shows variations of land cover type, air temperature, evapotranspiration (ET), and precipitation with elevation over the mountainous areas upstream of the HRB. The area of the four major vegetation types (i.e., cropland, forest, grassland, and shrubland) increases with the altitude in elevations ranging from 1000 to 3000 m. The patterns in vegetation cover are closely related to the precipitation variations. For altitudes ranging from 1000 to 3000 m, ET increases with elevation due to the increase in vegetation coverage and precipitation. The highest ET values occur at altitudes ranging from 2800 to 3200 m where vegetation coverage and precipitation reach their peak values. For elevations higher than 3000 m, precipitation and vegetation

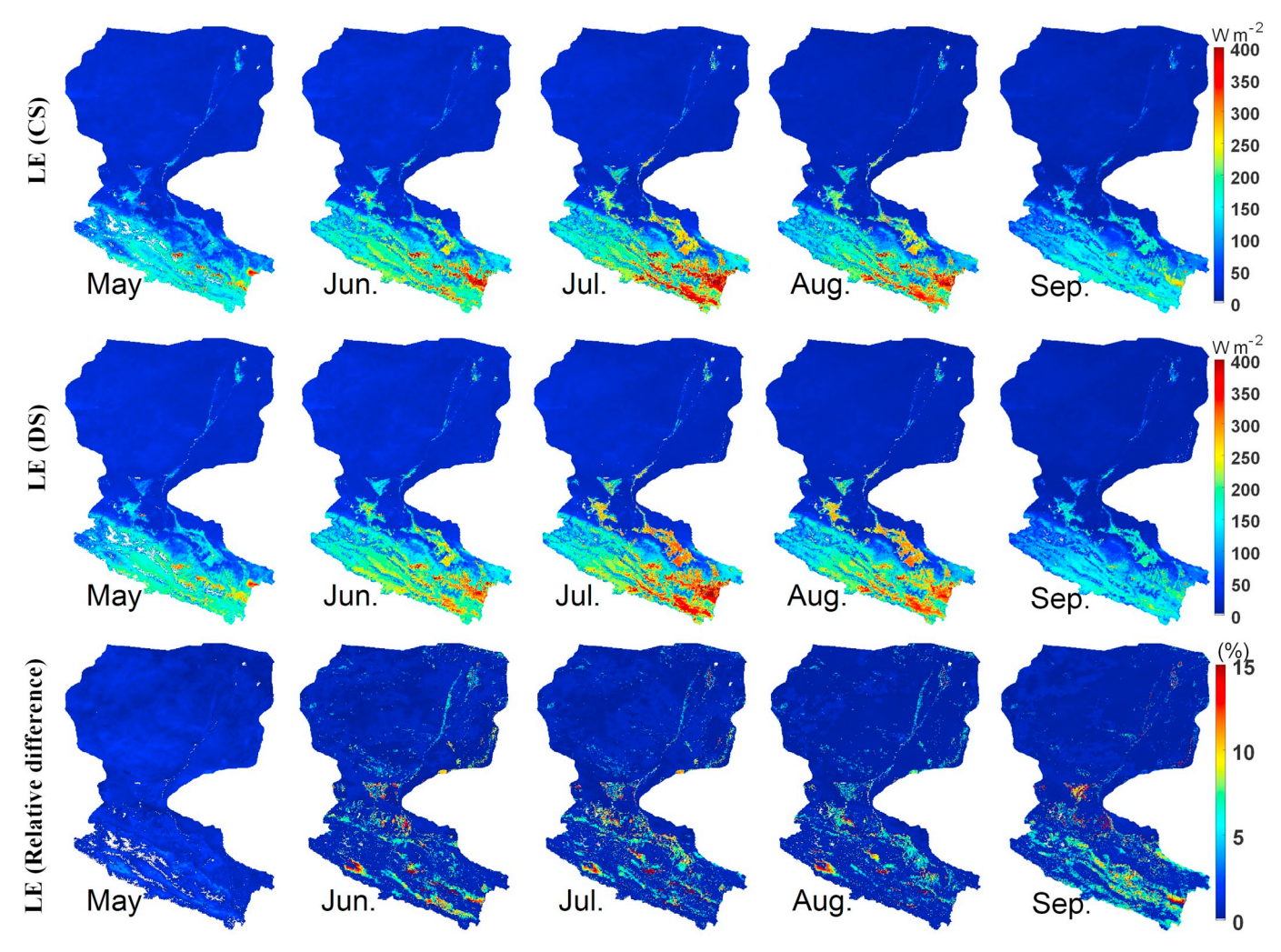
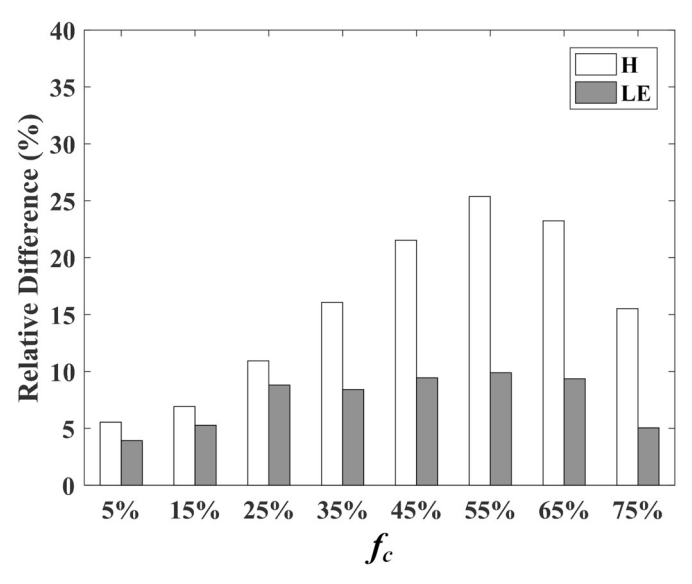


Fig. 10. Maps of monthly mean LE estimates from the CS (first row) and DS (second row) VDA approaches. The relative difference of LE estimates from the CS and DS models ((LE  $_{DS}$ - LE  $_{CS}$ )/LE  $_{DS}$  × 100) is shown in the third row. LE  $_{DS}$  and LE  $_{CS}$  denote the latent heat flux estimates from the DS and CS models, respectively.



**Fig. 11.** The relative difference of turbulent heat fluxes estimates from the CS and DS models for different vegetation fraction ( $f_c$ ) values.

coverage decrease, and consequently ET is reduced. The runoff flows from higher to lower altitudes, causing higher ET than precipitation at elevations  $<1600\,m.$  Fig. 12 also shows that the air temperature gradually decreases with the increase in elevation. The vegetation cover reaches its peak over the altitudes ranging from 2800 to 3200 m (where the air temperature is around 7 °C). This is consistent with Cui's (2013) finding that the optimal temperature for the vegetation growth in the Tibetan Plateau area is about 7 °C.

# 4.5. Effects of LST temporal sampling on the H and LE estimates

A number of numerical tests are conducted to evaluate the effect of LST temporal sampling on the partitioning of the available energy between the sensible and latent heat fluxes. Using different sampling strategies, the ground-measured LSTs in the Daman site are assimilated into the new (that uses EF values from Eq. (14) as the initial guess) and Bateni et al. (2013a) VDA models for DOYs 121–273, 2015.

The first numerical test is implemented by assimilating the LST observation once per day, which is sampled from the hourly LST measurements in the assimilation window (i.e., 0900 to 1800 LT). Fig. 13 shows the MAPE of H and LE estimates from this study (solid lines) and Bateni et al. (2013a) (dashed lines) for different LST assimilation times. H and LE estimates from this study have a lower MAPE

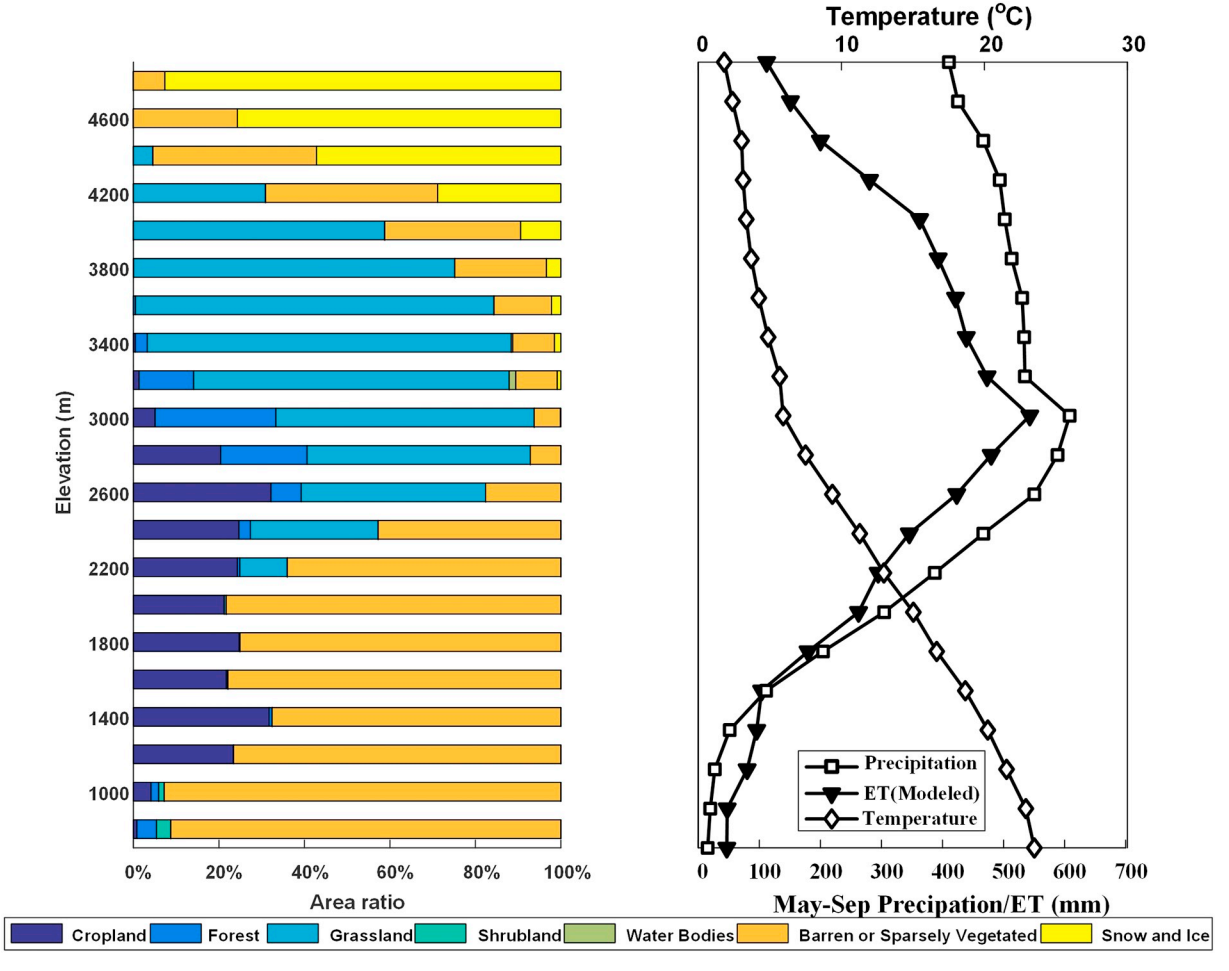
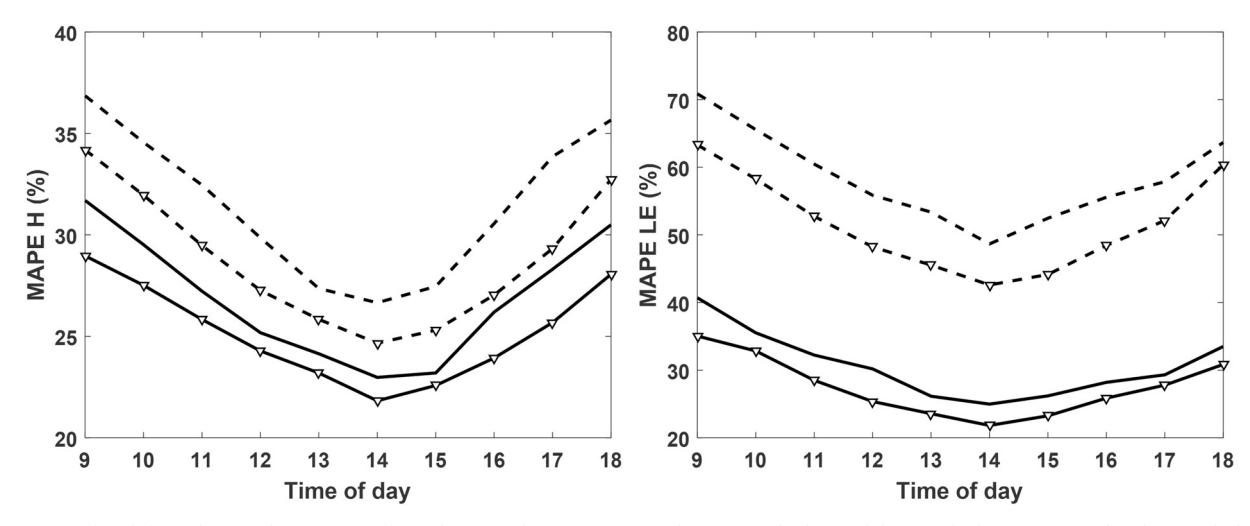


Fig. 12. Changes in land cover type, air temperature, ET, and precipitation with elevation over mountainous areas in the upstream of HRB in 2015.



**Fig. 13.** MAPEs of *H* (left) and LE (right) estimates from the CS and DS VDA approaches versus the hour of day in which LST is assimilated (in each day, LST is assimilated only once). The solid lines represent results from this study, and the dashed lines show results from Bateni et al. (2013a). Lines with symbols show results from the DS model, and lines without symbols indicate outcomes from the CS model.

than those from Bateni et al. (2013a) for all the LST assimilation times. As indicated in Fig. 13, the MAPEs of H and LE estimates reach the lowest value when the LST measurement at 14:00 LT is assimilated, implying that LST around noon has the most amount of information for partitioning the available energy between the sensible and latent heat

fluxes. This occurs because LST around noon reaches its maximum value, and hence has a vital role in characterizing the diurnal cycle of LST. When LST is assimilated at 1400 LT, the MAPEs of H and LE estimates from Bateni et al. (2013a) are 28.77% and 51.57%, respectively. By parameterizing EF in terms of  $\tau$  in this study, the MAPEs of H

**Table 4** Number (per day) and local time of assimilated LSTs.

Number of assimilated LSTs	Local time(s) of assimilated LSTs		
1	14:00 LT		
2	13:00-14:00 LT		
3	13:00-15:00 LT		
4	12:00-15:00 LT		
5	12:00-16:00 LT		
6	11:00-16:00 LT		
7	11:00-17:00 LT		
8	10:00-17:00 LT		
9	10:00-18:00 LT		
10	9:00–18:00 LT		

and LE estimates are reduced to 25.18% and 27.48%, respectively. Overall, the MAPEs of H and LE estimates from this study are less than those of Bateni et al. (2013a). This is due to the fact that our study parameterizes the a priori EF in terms of ATI and LAI via Eqs. (14), (15a) and (15b), and uses it as the initial guess in the VDA approach to obtain the a posteriori (optimal) EF estimate. While, Bateni et al. (2013a) did not characterize the a priori EF and used a constant value of 0.7 as the initial guess for EF in the VDA method. As expected, the MAPEs of H and LE estimates from the DS scheme are lower than those of the CS model.

The second numerical experiment assimilates LSTs at multiple times during each day (Table 4). For example, in the first attempt, LST is assimilated at 14:00 LT (the first row in Table 4), and in the second try, LSTs are assimilated at 13:00 and 14:00 LT (the second row in Table 4).

Fig. 14 shows the MAPEs of H and LE estimates by assimilating LST observations multiple times per day. In this figure, 1, 2, 3, ..., 10 imply that LST is assimilated once, twice, 3 times, ..., 10 times in each day, at the specified time(s) in Table 4. As anticipated, the MAPEs from the CS and DS VDA models are reduced by increasing the number of assimilated LST observations. The MAPEs of H and LE estimates decrease significantly when the number of assimilated LSTs increases from 1 to 3, but reduce slightly when there are > 3 LST assimilations per day. Also, the MAPE from this study is less than Bateni et al. (2013a), indicating that the VDA approach with a better initial guess for EF can perform more accurately.

#### 5. Conclusions

Turbulent heat fluxes are estimated by the variational assimilation of low temporal resolution land surface temperature (LST) data from polar orbiting satellites into both the combined-source (CS) and dual-source (DS) surface energy balance (SEB) schemes. An expression is developed to estimate an a priori EF in terms of leaf area index (LAI) and/or apparent thermal inertia (ATI). The a priori EF estimate is used in the VDA approach to find a posteriori (optimal) EF estimate.

The CS and DS VDA approaches are tested over the Heihe River Basin (HRB) in northwestern China, which samples a wide range of hydrological and vegetative conditions. The MODIS LST data with 1 km × 1 km spatial resolution and 2-revisit during the daytime are assimilated into the CS and DS VDA approaches. The results show that the neutral heat transfer coefficient  $(C_{HN})$  estimates increase with the increase of vegetation coverage fraction. Also, the spatial patterns of estimated daily soil evaporative fraction (EFs) maps are consistent with those of the Soil Moisture Active Passive (SMAP) soil moisture product. The estimated sensible and latent heat fluxes from the CS and DS VDA models are validated with the large aperture scintillometer (LAS) observations at the Arou (grassland), Daman (cropland), and Sidaoqiao (shrub-forest) sites in the upstream, midstream, and downstream of the HRB, respectively. For the CS VDA approach, the three-site-averaged root mean square error (RMSE) is 37.44 W m<sup>-2</sup> for sensible heat flux, and  $94.30\,\mathrm{W\,m^{-2}}$  for latent heat flux. The DS VDA model reduces the aforementioned RMSEs by 19.82% and 21.37% because it takes into account the interaction between the soil and the canopy. All of these results show that the proposed VDA approach performs well with the assimilation of low temporal resolution MODIS LST data in lieu of the high temporal resolution LST data from geostationary satellites.

The numerical experiments show that LST observations around noon (i.e., when LST reaches its maximum) have more information on the partitioning of the available energy between the turbulent heat fluxes. This happens because the maximum LST has a key role in characterizing the diurnal cycle of LST. The numerical experiments also indicate that the mean absolute percentage errors (MAPEs) of sensible and latent heat fluxes estimates decrease when the number of LST assimilations in each day increases. The MAPE from this study is less than that of Bateni et al. (2013a) if the same number of LST observations is assimilated. This indicates the new VDA approach can estimate the turbulent heat fluxes more accurately.

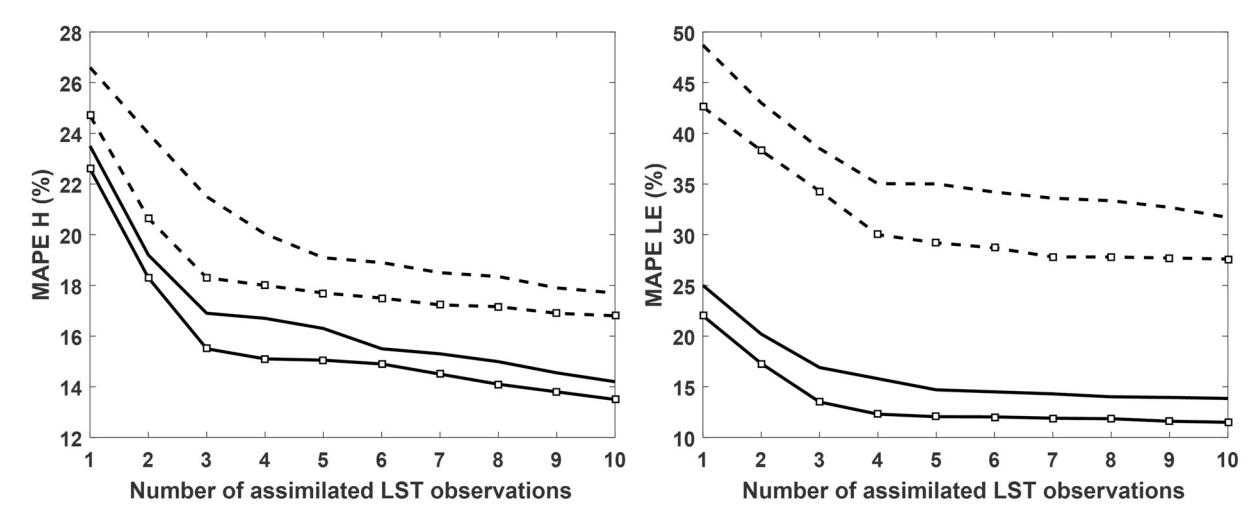


**Fig. 14.** MAPE of *H* (left) and LE (right) estimates from the CS and DS VDA approaches versus the number of assimilated LST observations. The solid lines represent results from this study, and the dashed lines show results from Bateni et al. (2013a). Lines with symbols show results from the DS model, and lines without symbols indicate outcomes from the CS model.

## Acknowledgment

The authors would like to thank all the scientists, engineers, and students who participated in the HiWATER field campaigns. This work was funded by the National Natural Science Foundation of China (grants 91425303, 41671335 and 91647104), and the United States Department of Agriculture-Natural Resources Conservation Service

(grant 69-3A75-17-54), and the United States Geological Service (grant 2017HI440B) awarded to the University of Hawaii at Manoa, as well as the State Key Laboratory of Earth Surface Processes and Resource Ecology (grant 2017-FX-04). This is contributed paper WRRC-CP-2019-08 of the Water Resources Research Center, University of Hawaii at Manoa, Honolulu, Hawaii.

# Appendix A

Table A1
The utilized symbols in equations of this study, and their definition.

Symbol	Definition
A	Amplitude of diurnal temperature cycle
ATI	Apparent thermal inertia
c	Soil heat capacity
$\mathfrak{c}_p$	Air heat capacity
C C	Solar correction factor
$C_H$	Heat transfer coefficient
C <sub>HN</sub>	Neutral heat transfer coefficient
C <sub>HS</sub>	Neutral heat transfer coefficients from leaves to air within the canop
SHS CHC	Neutral heat transfer coefficients from soil to air within the canopy
∽нс D	Heat diffusion coefficient
EF	Evaporative fraction
EF <sub>S</sub>	Soil evaporative fraction
EF <sub>C</sub>	Canopy evaporative fraction
f <sub>c</sub>	Vegetation cover fraction
G	Ground heat flux
Н	Sensible heat flux
$H_S$	Sensible heat flux for soil
$H_C$	Sensible heat flux for canopy
K	Soil heat conductivity
LAI	Leaf area index
LE	Latent heat flux
LEs	Latent heat flux for soil
LE <sub>C</sub>	Latent heat flux for canopy
LST	Land surface temperature
nd	Day number
Ri	Richardson number
	Net radiation
$R_N$	
R <sub>NS</sub>	Net radiation for soil
R <sub>NC</sub>	Net radiation for canopy
R <sub>S</sub> ↓	Incoming shortwave radiation
$R_L^{\downarrow}$	Incoming longwave radiation
T	Land surface temperature estimates from the heat diffusion equation
$\overline{\Gamma}$	Daily mean surface temperature
$T_a$	Air temperature
$T_{OBS}$	Land surface temperature observations
$T_S$	Soil temperature
$T_C$	Canopy temperature
$T_W$	Air temperature within the canopy
U.	Wind speed
$U_W$	Wind speed within the canopy
α	Surface albedo
-	Surface albedo for soil
$\alpha_s$	
$lpha_c$	Surface albedo for canopy
9	Surface emissivity
$e_{s}$	Soil emissivity
e <sub>c</sub>	Canopy emissivity
Ţ.	Stefan-Boltzmann constant
)	Air density
Þ	Latitude
φ	Calibration coefficient
τ	Environmental index
1	Lagrange multiplier
δ	Solar declination
Γ	Day angle
ω	Angular velocity of Earth's rotation
Ψ	Phase angle

#### References

- Abdolghafoorian, A., Farhadi, L., Bateni, S.M., Margulis, S., Xu, T.R., 2017. Characterizing the effect of vegetation dynamics on the bulk heat transfer coefficient to improve variational estimation of surface turbulent fluxes. J. Hydrometeorol. 18, 321–333. https://doi.org/10.1175/JHM-D-16-0097.1.
- Anderson, M.C., Norman, J.M., Diak, G.R., Kustas, W.P., Mecikalski, J.R., 1997. A two-source time-integrated model for estimating surface fluxes using thermal infrared remote sensing. Remote Sens. Environ. 60 (2), 195–216. https://doi.org/10.1016/S0034-4257(96)00215-5.
- Bastiaanssen, W.G.M., Menenti, M., Feddes, R.A., Holtslag, A.A.M., 1998a. A remote sensing surface energy balance algorithm for land (SEBAL): 1. Formulation. J. Hydrol. 212–213, 198–212. https://doi.org/10.1016/S0022-1694(98)00253-4.
- Bastiaanssen, W.G.M., Pelgrum, H., Wang, J., Ma, Y., Moreno, J.F., Roerink, G.J., van der Wal, T., 1998b. A remote sensing surface energy balance algorithm for land (SEBAL): 2. Validation. J. Hydrol. 212–213, 213–229. https://doi.org/10.1016/S0022-1694(98)00254-6.
- Bastiaanssen, W.G.M., Noordman, E.J.M., Pelgrum, H., Davids, G., Thoreson, B.P., Allen, R.G., 2005. SEBAL model with remotely sensed data to improve waterresources management under actual field conditions. J. Irrig. Drain. 131, 85–93.
- Bateni, S., Entekhabi, D., 2012a. Relative efficiency of land surface energy balance components. Water Resour. Res. 48, W04510. https://doi.org/10.1029/ 2011WR011357.
- Bateni, S., Entekhabi, D., 2012b. Surface heat flux estimation with the ensemble Kalman smoother: joint estimation of state and parameters. Water Resour. Res. 48, W08521. https://doi.org/10.1029/2011WR011542.
- Bateni, S.M., Liang, S., 2012. Estimating surface energy fluxes using a dual-source data assimilation approach adjoined to the heat diffusion equation. J. Geophys. Res. 117, D17118. https://doi.org/10.1029/2012JD017618.
- Bateni, S.M., Entekhabi, D., Jeng, D.S., 2013a. Variational assimilation of land surface temperature and the estimation of surface energy balance components. J. Hydrol. 481, 143–156. https://doi.org/10.1016/j.jhydrol.2012.12.039.
- Bateni, S.M., Entekhabi, D., Castelli, F., 2013b. Mapping evaporation and estimation of surface control of evaporation using remotely sensed land surface temperature from a constellation of satellites. Water Resour. Res. 49, 950–968. https://doi.org/10.1002/ wrcr.20071.
- Bateni, S.M., Entekhabi, D., Margulis, S., Castelli, F., Kergoat, L., 2014. Coupled estimation of surface heat fluxes and vegetation dynamics from remotely sensed land surface temperature and fraction of photosynthetically active radiation. Water Resour. Res. 50, 8420–8440. https://doi.org/10.1002/2013WR014573.
- Boni, G., Entekhabi, D., Castelli, F., 2001. Land data assimilation with satellite measurements for the estimation of surface energy balance components and surface control on evaporation. Water Resour. Res. 37 (6), 1713–1722. https://doi.org/10.1029/2001wr900020.
- Caparrini, F., Castelli, F., Entekhabi, D., 2003. Mapping of land atmosphere heat fluxes and surface parameters with remote sensing data. Bound.-Layer Meteorol. 107 (3), 605–633.
- Caparrini, F., Castelli, F., Entekhabi, D., 2004a. Estimation of surface turbulent fluxes through assimilation of radiometric surface temperature sequences. J. Hydrometeorol. 5, 145–159.
- Caparrini, F., Castelli, F., Entekhabi, D., 2004b. Variational estimation of soil and vegetation turbulent transfer and heat flux parameters from sequences of multisensor imagery. Water Resour. Res. 40, 1713–1722.
- Carrera, M., Belair, S., Bilodeau, B., 2015. The Canadian Land Data Assimilation System (CaLDAS): description and synthetic evaluation study. J. Hydrometeorol. 16, 1293–1314.
- Castelli, F., Entekhabi, D., Caporali, E., 1999. Estimation of surface heat transfer and an index of soil moisture using adjoint-state surface energy balance. Water Resour. Res. 35, 3115–3126.
- Chen, S.X., 2008. Thermal conductivity of sands. Heat Mass Transf. 44 (10), 1241–1246. https://doi.org/10.1007/s00231-007-0357-1.
- Crago, R.D., 1996. Conservation and variability of the evaporative fraction during the daytime. J. Hydrol. 180 (1–4), 173–194. https://doi.org/10.1016/0022-1694(95) 02903-6.
- Crow, W.T., Kustas, W.P., 2005. Utility of assimilating surface radiometric temperature observations for evaporative fraction and heat transfer coefficient retrieval. Bound.-Layer Meteorol. 115 (1), 105–130. https://doi.org/10.1007/s10546-004-2121-0.
- Cui, Y.P., 2013. Preliminary estimation of the realistic optimum temperature for vegetation growth in China. Environ. Manag. 52, 151–162.
- de Vries, D.A., 1963. Thermal properties of soils. In: van Wijk, W.R. (Ed.), Physics of Plant Environment. North-Holland, Amsterdam, pp. 210–235.
- Dirmeyer, P.A., Zeng, F.J., Ducharne, A., Morrill, J.C., Koster, R.D., 2000. The sensitivity of surface fluxes to soil water content in three land surface schemes. J. Hydrometeorol. 1 (2), 121–134.
- Fourier, J.B.J., 1822. Theorie Analytique de la Chaleur. F. Didot, Paris, France.
- Gentine, P., Entekhabi, D., Chehbouni, A., Boulet, G., Duchemin, B., 2007. Analysis of evaporative fraction diurnal behaviour. Agric. For. Meteorol. 143 (1–2), 13–29. https://doi.org/10.1016/j.agrformet.2006.11.002.
- Hu, Z., Islam, S., 1995. Prediction of ground temperature and soil moisture content by the force–restore method. Water Resour. Res. 31, 2531–2539. https://doi.org/10.1029/ 95WR01650.
- Jia, L., Xi, G., Liu, S., Huang, C., Yan, Y., Liu, G., 2009. Regional estimation of daily to annual regional evapotranspiration with MODIS data in the Yellow River Delta wetland. Hydrol. Earth Syst. Sci. 13, 1775–1787.
- Jiang, L., Islam, S., 2001. Estimation of surface evaporation map over Southern Great

- Plain using remote sensing data. Water Resour. Res. 37 (2), 329-340.
- Jiang, L., Islam, S., 2003. An intercomparison of regional latent heat flux estimation using remote sensing data. Int. J. Remote Sens. 24 (11), 2221–2236.
- Kustas, W.P., Norman, J.M., 1999. Evaluation of soil and vegetation heat flux predictions using a simple two-source model with radiometric temperatures for partial canopy cover. Agric. For. Meteorol. 94, 13–29.
- Kustas, W.P., Humes, K.S., Norman, J.M., Moran, M.S., 1996. Single- and dual-source modeling of surface energy fluxes with radiometric surface temperature. J. Appl. Meteorol. 35 (1), 110–121.
- Li, X., Cheng, G., Liu, S., 2013. Heihe watershed allied telemetry experimental research (HiWATER): scientific objectives and experimental design. Bull. Am. Meteorol. Soc. 94 (8), 1145–1160.
- Li, Y., Huang, C., Hou, J., Gu, J., Zhu, G., Li, X., 2017. Mapping daily evapotranspiration based on spatiotemporal fusion of ASTER and MODIS images over irrigated agricultural areas in the Heihe River Basin, Northwest China. Agric. For. Meteorol. 244–245, 82–97.
- Li, X., Liu, S., Li, H., Ma, Y., Wang, J., Zhang, Y., Xu, Z., Xu, T., Song, L., Yang, X., Lu, Z., Wang, Z., Guo, Z., 2018. Intercomparison of six upscaling evapotranspiration methods: from site to the satellite pixel. J. Geophys. Res. Atmos. 123, 6777–6803. https://doi.org/10.1029/2018JD028422.
- Liu, S.M., Hu, G., Lu, L., 2007. Estimation of regional evapotranspiration by TM/ETM+ data over heterogeneous surfaces. Photogramm. Eng. Remote. Sens. 73, 1169–1178.
- Liu, S.M., Xu, Z.W., Wang, W.Z., Jia, Z.Z., Zhu, M.J., Wang, J.M., 2011. A comparison of eddy-covariance and large aperture scintillometer measurements with respect to the energy balance closure problem. Hydrol. Earth Syst. Sci. 15, 1291–1306.
- Liu, S.M., Xu, Z.W., Song, L.S., Zhao, Q.Y., Xu, T.R., Ge, Y., Ma, Y.F., Zhu, Z.L., Jia, Z.Z., Zhang, F., 2016. Upscaling evapotranspiration measurements from multi-site to the satellite pixel scale over heterogeneous land surfaces. Agric. For. Meteorol. 230–231, 97–113. https://doi.org/10.1016/j.agrformet.2016.04.008.
- Lu, Y., Steele-Dunne, S.C., Farhadi, L., van de Giesen, N., 2017. Mapping surface heat fluxes by assimilating SMAP soil moisture and GOES land surface temperature data. Water Resour. Res. 53 (12), 10858–10877.
- Ma, Y., Liu, S., Song, L., Xu, Z., Liu, Y., Xu, T., Zhu, T., 2018. Estimation of daily evapotranspiration and irrigation water efficiency at a Landsat-like scale for an arid irrigation area using multi-source remote sensing data. Remote Sens. Environ. 216, 715–734. https://doi.org/10.1016/j.rse.2018.07.019.
- Mallick, K., Jarvis, A.J., Fisher, J.B., Tu, K.P., Boegh, E., Niyogi, D., 2013. Latent heat flux and canopy conductance based on Penman-Monteith, Priestly-Taylor equation, and Bouchets complementary hypothesis. J. Hydrometeorol. 14, 419–442. https://doi. org/10.1175/JHM-D-12-0117.1.
- Mallick, K., Jarvis, A.J., Boegh, E., Fisher, J.B., Drewry, D.T., Tu, K.P., Hook, S.J., Hulley, G., Ardö, J., Beringer, J., Arain, A., Niyogi, D., 2014. A surface temperature initiated closure (STIC) for surface energy balance fluxes. Remote Sens. Environ. 141, 243–261.
- Nishida, K., Nemani, R.R., Glassy, J.M., Running, S.W., 2003. Development of an evapotranspiration Index from Aqua/MODIS for monitoring surface moisture status. IEEE Geosci. Remote Sens. Lett. 41 (2), 493–500.
- Norman, J.M., Becker, F., 1995. Terminology in thermal infrared remote sensing of natural surfaces. Agric. For. Meteorol. 77, 153–166.
- Norman, J.M., Kustas, W.P., Humes, K., 1995. Source approach for estimating soil and vegetation energy fluxes in observations of directional radiometric surface temperature. Agric. For. Meteorol. 77, 263–293.
- Pan, X.D., Li, X., Shi, X.K., Han, X.J., Luo, L.H., Wang, L.X., 2012. Dynamic downscaling of near-surface air temperature at the basin scale using WRF-a case study in the Heihe river basin, China. Front. Earth Sci. 6 (3), 314–323.
- Peters-Lidard, C.D., Kumar, S.V., Mocko, D.M., Tian, Y., 2011. Estimating evapotranspiration with land data assimilation systems, hydrological processes. Hydrol. Process. 25 (26), 3979–3992. https://doi.org/10.1002/hyp.8387.
- Qin, J., Liang, S., Liu, R., Zhang, H., Hu, B., 2007. A weak-constraint based data assimilation scheme for estimating surface turbulent fluxes. IEEE Geosci. Remote Sens. Lett. 4 (4), 649–653. https://doi.org/10.1109/LGRS.2007.904004.
- Qin, J., Yang, K., Lu, N., Chen, Y., Zhao, L., Han, M., 2013. Spatial upscaling of in-situ soil moisture measurements based on MODIS-derived apparent thermal inertia. Remote Sens. Environ. 138 (1–9).
- Shokri, N., Lehmann, P., Vontobel, P., Or, D., 2008a. Drying front and water content dynamics during evaporation from sand delineated by neutron radiography. Water Resour. Res. 44, W06418. https://doi.org/10.1029/2007wr006385.
- Shokri, N., Lehmann, P., Or, D., 2008b. Characteristics of evaporation from partially wet table porous media. Water Resour. Res. 45, W02415. https://doi.org/10.1029/ 2008wr007185.
- Short, N., Stuart Jr., L., 1982. The Heat Capacity Mapping Mission (HCMM) Anthology. Tech. rep., NASA.
- Sini, F., Boni, G., Caparrini, F., Entekhabi, D., 2008. Estimation of large-scale evaporation fields based on assimilation of remotely sensed land temperature. Water Resour. Res. 44, W06410. https://doi.org/10.1029/2006WR005574.
- Song, L.S., Kustas, W.P., Liu, S.M., Colaizzi, P.D., Nieto, H., Xu, Z.W., Ma, Y.F., Li, M.S., Xu, T.R., Agam, N., Tolk, J.A., Evett, S.R., 2016a. Applications of a thermal-based two-source energy balance model using Priestley-Taylor approach for surface temperature partitioning under advective conditions. J. Hydrol. 540, 574–587. https://doi.org/10.1016/j.jhydrol.2016.06.034.
- Song, X., Liu, F., Zhang, G., Li, D., Zhao, Y., 2016b. Estimation of soil texture at a regional scale using local soil-landscape models. Soil Sci. 181, 435–445.
- Su, Z., 2002. The Surface Energy Balance System (SEBS) for estimation of turbulent heat fluxes. Hydrol. Earth Syst. Sci. 6, 85–100. https://doi.org/10.5194/hess-6-85-2002.
- Sun, L., Liang, S., Yuan, W., Chen, Z., 2013. Improving a Penman–Monteith evapotranspiration model by incorporating soil moisture control on soil evaporation in

- semiarid areas. Int. J. Digital Earth 6 (1), 134-156.
- Tang, R., Li, Z.L., Tang, B., 2010. An application of the Ts-VI triangle method with enhanced edges determination for evapotranspiration estimation from MODIS data in arid and semi-arid regions: implementation and validation. Remote Sens. Environ. 114. 540-551.
- Twine, T.E., Kustas, W.P., Norman, J.M., Cook, D.R., Houser, P.R., Meyers, T.P., Prueger, J.H., Starks, P.J., Wesely, M.L., 2000. Correcting eddy-covariance flux underestimates over grassland. Agric. For. Meteorol. 103, 279–300.
- Van doninck, J., Peters, J., Baets, B.D., Clercq, E.M.D., Ducheyne, E., Verhoest, N.E.C., 2011. The potential of multitemporal aqua and Terra MODIS apparent thermal inertia as a soil moisture indicator. Int. J. Appl. Earth Obs. Geoinf. 13, 934–941.
- Verstraeten, W.W., Veroustraete, F., van der Sande, C.J., Grootaers, I., Feyen, J., 2006. Soil moisture retrieval using thermal inertia, determined with visible and thermal spaceborne data, validated for European forests. Remote Sens. Environ. 101, 290-314
- Voogt, J.A., Grimmond, C.S.B., 2000. Modeling surface sensible heat flux using surface radiative temperatures in a simple urban area. J. Appl. Meteorol. 39, 1679–1699.
- Wang, K., Li, Z., Cribb, M., 2006. Estimating of evaporative fraction from a combination of day and night land surface temperature and NDVI: a new method to determine the Priestley-Taylor parameter. Remote Sens. Environ. 102, 293–305. https://doi.org/10. 1016/j.rse.2006.02.007.
- Williams, I.N., Lu, Y., Kueppers, L.M., Riley, W.J., Biraud, S.C., Bagley, J.E., Torn, M.S., 2016. Land-atmosphere coupling and climate prediction over the US Southern Great Plains. J. Geophys. Res. Atmos. 121, 12125–12144.
- Xia, Y., Sheffield, J.S., Ek, M.B., Dong, J., Chaney, N., Wei, H., Meng, J., Wood, E.F., 2014a. Evaluation of multi-model simulated soil moisture in NLDAS-2. J. Hydrol. 512, 107–125. https://doi.org/10.1016/j.jhydrol.2014.02.027.
- Xia, Y., Ek, M., Mocko, D., Peters-Lidard, C., Sheffield, J., Dong, J., Wood, E., 2014b. Uncertainties, correlations, and optimal blends of drought indices from the NLDAS multiple land surface model ensemble. J. Hydrometeorol. https://doi.org/10.1175/ JHM-D-13-058.1.
- Xiao, Z., Liang, S., Wang, J., Chen, P., Yin, X., Zhang, L., Song, J., 2014. Use of general regression neural networks for generating the GLASS leaf area index product from time-series MODIS surface reflectance. IEEE Trans. Geosci. Remote Sens. 52 (1), 209–223.
- Xiao, Z., Liang, S., Wang, J., Xiang, Y., Zhao, X., Song, J., 2016. Long-time-series global land surface satellite leaf area index product derived from MODIS and AVHRR surface reflectance. IEEE Trans. Geosci. Remote Sens. 54 (9), 5301–5318.
- Xu, T., Liu, S.M., Liang, S., Qin, J., 2011a. Improving predictions of water and heat fluxes by assimilating MODIS land surface temperature products into common land model. J. Hydrometeorol. 12, 227–244.
- Xu, T., Liang, S., Liu, S., 2011b. Estimating turbulent fluxes through assimilation of geostationary operational environmental satellites data using ensemble Kalman filter. J. Geophys. Res. Atmos. 116, D09109. https://doi.org/10.1029/2010JD015150.

- Xu, Z., Liu, S., Li, X., Shi, S., Wang, J., Zhu, Z., Xu, T.R., Wang, W., Ma, M., 2013. Intercomparison of surface energy flux measurement systems used during the HiWATER-MUSOEXE. J. Geophys. Res. Atmos. 118 (23), 13140–13157.
- Xu, T., Bateni, S.M., Liang, S., Entekhabi, D., Mao, K.B., 2014. Estimation of surface turbulent heat fluxes via variational assimilation of sequences of land surface temperatures from Geostationary Operational Environmental Satellites. J. Geophys. Res. Atmos. 119. 10780–10798.
- Xu, T., Liu, S.M., Xu, Z.W., Liang, S., Xu, L., 2015a. A dual-pass data assimilation scheme for estimating surface fluxes with FY3A-VIRR land surface temperature. Sci. China Earth Sci. 58, 211–230. https://doi.org/10.1007/s11430-014-4964-7.
- Xu, T., Bateni, S.M., Liang, S., 2015b. Estimating turbulent heat fluxes with a weak-constraint data assimilation scheme: a case study (HiWATER-MUSOEXE). IEEE Geosci. Remote Sens. Lett. 12, 68–72.
- Xu, T., Bateni, S.M., Margulis, S.A., Song, L., Liu, S.M., Xu, Z.W., 2016. Partitioning evapotranspiration into soil evaporation and canopy transpiration via a two-source variational data assimilation system. J. Hydrometeorol. 17, 2353–2370. https://doi. org/10.1175/JHM-D-15-0178.1.
- Xu, T., Bateni, S.M., Neale, C.M.U., Auligne, T., Liu, S., 2018a. Estimation of turbulent heat fluxes by assimilation of land surface temperature observations from GOES satellites into an ensemble Kalman smoother framework. J. Geophys. Res. Atmos. 123, 2409–2423. https://doi.org/10.1002/2017JD027732.
- Xu, T., Guo, Z., Liu, S., He, X., Meng, Y., Xu, Z., et al., 2018b. Evaluating different machine learning methods for upscaling evapotranspiration from flux towers to the regional scale. J. Geophys. Res. Atmos. 123. https://doi.org/10.1029/2018.ID028447.
- Yao, Y., Liang, S., Cheng, J., Liu, S., Fisher, J.B., Zhang, X., Jia, K., Zhao, X., Qin, Q., Zhao, B., 2013. MODIS-driven estimation of terrestrial latent heat flux in China based on a modified Priestley-Taylor algorithm. Agric. For. Meteorol. 171–172, 187–202.
- Zhang, X., Liang, S., Zhou, G., Wu, H., Zhao, X., 2014. Generating global land surface satellite incident shortwave radiation and photosynthetically active radiation products from multiple satellite data. Remote Sens. Environ. 152, 318–332.
- Zhong, B., Ma, P., Nie, A.H., Yang, A.X., Yao, Y.J., Lv, W.B., Zhang, H., Liu, Q.H., 2014. Land cover mapping using time series HJ-1/CCD data. Sci. China Earth Sci. 57 (8), 1790–1799.
- Zhong, B., Yang, A., Nie, A., Yao, Y., Zhang, H., Wu, S., Liu, Q., 2015. Finer resolution land-cover mapping using multiple classifiers and multisource remotely sensed data in the Heihe river basin. IEEE J. STARS. 8, 4973–4992.
- Zhou, C., Wang, K., 2016. Biological and environmental controls on evaporative fractions at AmeriFlux sites. J. Appl. Meteorol. Climatol. 55 (1), 145–161. https://doi.org/10. 1175/JAMC-D-15-0126.1.
- Zhu, W., Jia, S., Lv, A., 2017. A universal Ts-VI triangle method for the continuous retrieval of evaporative fraction from MODIS products. J. Geophys. Res. Atmos. 122, 10206–10227. https://doi.org/10.1002/2017JD026964.